11

FINITE DIFFERENCE METHOD FOR ELECTROMAGNETIC SCATTERING PROBLEMS

C. F. Lee, R. T. Shin, and J. A. Kong

11.1 Introduction

Finite difference techniques have been applied to analyze various electromagnetic problems in both frequency and time domains. Examples of these applications include scattering and radiation [1–19], microwave and millimeter wave circuits [24-25], and hyperthermia [22, 23]. Besides the widespread applications, the latest research efforts have been directed at achieving more accurate discretization schemes, improving absorbing boundary conditions for open region problems, and efficient implementations on supercomputers. In this chapter, three topics relevant to the finite difference technique are discussed: absorbing boundary conditions, spatial discretization, and time domain model for dispersive materials.

In the first section, the absorbing boundary conditions on circular and elliptical boundaries are discussed. The absorbing boundary conditions are crucial for open region problems such as scattering and radiation. The absorbing boundary conditions are used to simulate the unbounded space, and hence, provide finite computational domain for open region problems. The size of the computational domain is directly related to the absorbability of the absorbing boundary condition. The absorbing boundary condition will be derived based on the factorization of wave equation using pseudo-differential operator technique. The factorization scheme presented by Engquist and Majda [30] will be modified to derive absorbing boundary conditions for circular and elliptical boundaries. In the case of circular boundary, the modified factorization scheme will yield results equivalent to that of Bayliss and Turkel [33]. In the case of elliptical boundary, the absorbing boundary condition will be derived and numerically demonstrated to be efficient in reducing the size of the computational domain for elongated scatterers.

In the second section, a finite-difference time-domain (FD-TD) scheme on triangular grids is discussed. The discretization scheme is crucial in geometrical modeling, treating dielectric/magnetic materials, and efficient implementation. The discretization scheme is based on the combination of the finite difference and control region approximations [9]. The flexibility of the triangular grid is utilized to provide accurate geometrical modeling. It will be demonstrated that the FD-TD technique on triangular grid provides more accurate target modeling capability than the traditional FD-TD technique of the rectangular

grid.

In the third section, an efficient FD-TD algorithm for treating frequency dispersive material is presented. Accurate and efficient time domain model of dispersive materials is very important in time domain analysis. Accurate time domain results cannot be obtained unless the dispersive nature of the material is properly modeled. Traditional model of the dispersive characteristic is based on the time domain convolution integral which requires large memory and long computation time. More recent model is based on the exponential approximation of the time domain response of the material. In this section, we model the dispersive characteristics using ordinary time differential equations and provide an efficient discretization scheme.

11.2 Absorbing Boundary Conditions on Circular and Elliptical Boundaries

In the method of moments, the formulation is applied within or on the scatterer. The implication is that the number of unknowns is proportional to the volume or the surface area of the scatterer. On the other hand, finite difference methods are formulated in the entire space. Therefore, an outer boundary must be used to achieve a finite computational domain. The boundary condition placed on the outer boundary should simulate unbounded space and only permit outgoing scattered waves.

The boundary conditions [28-50] used on the outer boundary may be exact or approximate. The exact boundary conditions, such as the modal expansion [28] or the radiation integral [29] approach, require substantial memory and computation time [30,33]. The approximate boundary conditions [30,33] have been used widely, and are known to be efficient and offer sufficient accuracy.

Engquist and Majda [30] used the pseudo-differential operator [52-54] approach to obtain boundary conditions for rectangular and circular boundaries. The rectangular boundary operator has been applied to many problems [30,32], but suffers a drawback in that the normal at the corner is not defined. The boundary conditions for a circular outer boundary does not have the problem of undefined normals and has received wide attention in applications to both frequency and time domain problems.

For a circular boundary, Bayliss and Turkel [33] derived a boundary operator by assuming the Wilcox type expansion [51] for the scattered fields and then developing a series operator to eliminate the inverse power series. The most widely used operator is the second-order operator, which has been demonstrated to be effective in bringing the outer boundary closer to the scatterer, thus reducing the size of the computational domain. Also, it has been demonstrated to have higher absorbability than the corresponding Engquist and Majda condition [9].

In this section, the pseudo-differential operator approach is modified to derive an improved circular boundary condition [39]. The modified pseudo-differential operator approach is then used to derive the second-order absorbing boundary conditions for the elliptical outer boundary. The effectiveness of the elliptical boundary in reducing the size of the computational domain for elongated scatterers is illustrated by calculating bistatic and monostatic radar cross sections of a conducting ellipse, a strip, and a hypothetical "airfoil". In the following subsections, the time dependence $e^{-i\omega t}$ is assumed.

a. Absorbing Boundary Condition on Circular Boundary

The pseudo-differential operator approach provides a systematic way to obtain absorbing boundary conditions in orthogonal coordinate systems. This technique has been employed by Engquist and Majda [30] to derive absorbing boundary conditions for both circular and rectangular boundaries. We begin with an outline of [30]. Then, following a simple observation, we apply a straightforward modification to obtain an absorbing boundary condition which is equivalent to [33]. The pseudo-differential operator approach is best described in the Fourier transform domain of the transverse coordinates, but the results are identical if we treat the transverse derivative operator as an algebraic quantity.

Consider a two-dimensional (2D) scattering problem where the scattered field U_s is governed by 2D Helmholtz equation:

$$\left(\frac{\partial^2}{\partial r^2}+\frac{1}{r}\frac{\partial}{\partial r}+\frac{1}{r^2}\frac{\partial^2}{\partial \phi^2}+k^2\right)U_s=0 \tag{11.2.1}$$

We define:

$$L=\frac{\partial^2}{\partial r^2}+\frac{1}{r}\frac{\partial}{\partial r}+\frac{1}{r^2}\frac{\partial^2}{\partial \phi^2}+k^2 \tag{11.2.2}$$

Using the factorization theorem [52-54], the L operator is factored

into a product of incoming and outgoing wave operators as follows:

$$L = \left(\frac{\partial}{\partial r} + \lambda_+\right)\left(\frac{\partial}{\partial r} - \lambda_-\right) \tag{11.2.3}$$

where λ_+ and λ_- are functions of k, r and $\partial/\partial\phi$. The operator in the first parenthesis is the incoming wave operator while that in the second parenthesis is the outgoing wave operator which is an absorbing boundary operator:

$$\left(\frac{\partial}{\partial r} - \lambda_-\right) U_s = 0 \tag{11.2.4}$$

Hence, we need to find λ_-. Following [30], we expand λ_- into the following series:

$$\lambda_- = \lambda_-^{(1)} + \lambda_-^{(0)} + \ldots + \lambda_-^{(-n)} \tag{11.2.5}$$

in which $\lambda_-^{(j)}$ are recursively determined. To obtain the second order boundary operator, we need only the first two terms which are given by

$$\lambda_-^{(1)} = ik\sqrt{1 + \frac{1}{k^2r^2}\frac{\partial^2}{\partial\phi^2}} \sim ik\left(1 + \frac{1}{2k^2r^2}\frac{\partial^2}{\partial\phi^2}\right) \tag{11.2.6}$$

$$\lambda_-^{(0)} = -\frac{1}{2r} + \frac{1}{2r^3k^2}\frac{\partial^2}{\partial\phi^2} \tag{11.2.7}$$

The second-order boundary operator, obtained by combining (11.2.6) and (11.2.7), is

$$\frac{\partial}{\partial r} = ik - \frac{1}{2r} + \frac{1}{2k^2r^2}\left(ik + \frac{1}{r}\right)\frac{\partial^2}{\partial\phi^2} \tag{11.2.8}$$

These are the results obtained in [30]. By ignoring terms involving $1/r^2$ and higher-order terms from the second-order boundary operator, Sommerfeld's radiation condition can be obtained.

The first and second-order boundary operators derived by Bayliss and Turkel are given by [33]

$$\frac{\partial}{\partial r} = ik - \frac{1}{2r} \tag{11.2.9}$$

$$\frac{\partial}{\partial r} = \frac{1}{1+\frac{i}{kr}}\left(ik - \frac{3}{2r} - \frac{3i}{8kr^2} + \frac{i}{2kr^2}\frac{\partial^2}{\partial\phi^2}\right)$$
$$= ik - \frac{1}{2r} + \frac{ik}{2(kr)^2}\frac{\frac{\partial^2}{\partial\phi^2}+\frac{1}{4}}{1-\frac{1}{ikr}} \tag{11.2.10}$$

Equation (11.2.8) and (11.2.10) have been applied to many problems and it has been demonstrated [9] that (11.2.10) provides higher absorbability than (11.2.8).

In an attempt to improve the Engquist and Majda absorbing boundary condition, we recall Sommerfeld's radiation condition:

$$\frac{\partial}{\partial r} = ik - \frac{1}{2r} \tag{11.2.11}$$

The above equation ensures that, in the far field, the scattered waves are cylindrical waves. We notice that the Sommerfeld radiation condition appears in the first-order condition of the Bayliss and Turkel's results. On the other hand, the ik term appears in (11.2.6) while $1/2r$ appears in (11.2.7). Thus, Sommerfeld's radiation condition cannot be obtained by using (11.2.6) alone, and this observation motivates us to modify the approach in [30] and to group the ik and $1/2r$ terms.

Considering an arbitrary function of r, we have the following operator relationship:

$$\left(\frac{\partial}{\partial r}+\frac{1}{2r}\right)^2 + \frac{1}{4r} = \frac{\partial^2}{\partial r^2} + \frac{1}{r}\frac{\partial}{\partial r} \tag{11.2.12}$$

Substituting (11.2.12) into (11.2.2), we obtain

$$L = \left(\frac{\partial}{\partial r}+\frac{1}{2r}\right)^2 + k^2 + \frac{1}{r^2}\frac{\partial^2}{\partial\phi^2} + \frac{1}{4r^2} \tag{11.2.13}$$

Now we attempt to factor L into the following form:

$$L = \left(\frac{\partial}{\partial r}+\frac{1}{2r}+\lambda_+\right)\left(\frac{\partial}{\partial r}+\frac{1}{2r}-\lambda_-\right) \tag{11.2.14}$$

In order to find λ_-, we multiply out (11.2.14) and obtain

$$L = \frac{\partial^2}{\partial r^2} + \frac{1}{r}\frac{\partial}{\partial r} - \frac{1}{4r^2} + \frac{1}{2r}(\lambda_+ - \lambda_-) + (\lambda_+ - \lambda_-)\frac{\partial}{\partial r}$$
$$- \frac{\partial\lambda_-}{\partial r} - \lambda_+\lambda_- \tag{11.2.15}$$

By comparing (11.2.15) with (11.2.1), we have

$$\frac{1}{r^2}\frac{\partial^2}{\partial\phi^2} + k^2 = -\frac{1}{4r^2} + \frac{1}{2r}(\lambda_+ - \lambda_-) + (\lambda_+ - \lambda_-)\frac{\partial}{\partial r} - \frac{\partial\lambda_-}{\partial r} - \lambda_+\lambda_- \tag{11.2.16}$$

Since the left-hand-side of the above equation does not involve $\partial/\partial r$, we assume

$$\lambda_+ = \lambda_- = \lambda \tag{11.2.17}$$

and obtain

$$\frac{1}{r^2}\frac{\partial^2}{\partial\phi^2} + k^2 + \frac{1}{4r^2} = -\frac{\partial\lambda}{\partial r} - \lambda\lambda \tag{11.2.18}$$

To obtain the second order operator, we approximate λ by

$$\lambda \sim \lambda^{(1)} + \lambda^{(0)}. \tag{11.2.19}$$

where the leading terms of $\lambda^{(1)}$ and $\lambda^{(0)}$ are $O(1)$ and $O(1/r^3)$, respectively. They are determined recursively by inserting (11.2.19) into (11.2.18). For $\lambda^{(1)}$, we equate the left-hand-side of (11.2.18) to the terms for which the leading terms are $O(1)$. Assuming $\partial\lambda^{(1)}/\partial r$ is $O(1/r^3)$ [justified by (11.2.21)], we have:

$$\frac{1}{r^2}\frac{\partial^2}{\partial\phi^2} + k^2 + \frac{1}{4r^2} = -\lambda^{(1)}\lambda^{(1)} \tag{11.2.20}$$

Therefore,

$$\begin{aligned}\lambda^{(1)} &= ik\sqrt{1 + \frac{1}{k^2r^2}\frac{\partial^2}{\partial\phi^2} + \frac{1}{4k^2r^2}} \\ &\sim ik\left(1 + \frac{1}{2k^2r^2}\frac{\partial^2}{\partial\phi^2} + \frac{1}{8k^2r^2}\right)\end{aligned} \tag{11.2.21}$$

For $\lambda^{(0)}$, we set the terms for which the leading terms are $O(1/r^3)$ to zero.

$$-\frac{\partial\lambda^{(1)}}{\partial r} - \lambda^{(1)}\lambda^{(0)} - \lambda^{(0)}\lambda^{(1)} = 0 \tag{11.2.22}$$

We cannot, in general, assume that $\lambda^{(1)}$ and $\lambda^{(0)}$ commute. But keeping in mind that the transverse derivatives are algebraic quantities, since we are in the Fourier transform domain, we have:

$$\lambda^{(0)} = -\frac{1}{2\lambda^{(1)}}\frac{\partial\lambda^{(1)}}{\partial r} \tag{11.2.23}$$

Retaining the leading term for $\lambda^{(1)}$ in the denominator, we obtain

$$\lambda^{(0)} = \frac{1}{2k^2r^3}\left(\frac{\partial^2}{\partial\phi^2} + \frac{1}{4}\right) \tag{11.2.24}$$

By adding (11.2.21) and (11.2.24), we obtain λ_-, and consequently

$$\frac{\partial}{\partial r} = ik - \frac{1}{2r} + \frac{ik}{2(kr)^2}\left(1 + \frac{1}{ikr}\right)\left(\frac{\partial^2}{\partial\phi^2} + \frac{1}{4}\right) \tag{11.2.25}$$

The above equation is the new absorbing boundary condition, which is similar to (11.2.10). By substituting (11.2.25) into the Helmholtz equation, it can be shown that the leading residual term is proportional to $1/r^4$. In fact the simple algebraic approximation for large kr

$$1 + \frac{1}{ikr} \sim \frac{1}{1 - \frac{1}{ikr}} \tag{11.2.26}$$

converts (11.2.25) into (11.2.10).

b. Absorbing Boundary Condition on Elliptical Boundary

In this subsection we apply the pseudo-differential operator approach to find an absorbing boundary condition for elliptical boundaries. For elongated scatterers, the elliptical outer boundary may be used to reduce the size of the computational domain.

The 2D Helmholtz equation in elliptical coordinates is given by

$$\frac{4}{d^2\left[\cosh^2 u - \cos^2 v\right]}\left(\frac{\partial^2}{\partial u^2} + \frac{\partial^2}{\partial v^2}\right) U_s + k^2 U_s = 0 \tag{11.2.27}$$

where d is the interfocal distance and u, v are parameters of the elliptical coordinate system (Fig. 11.2.1). The parameters u and v are related to the rectangular coordinates by

$$x = \frac{d}{2}\cosh u \cos v, \qquad y = \frac{d}{2}\sinh u \sin v \tag{11.2.28}$$

in which $0 \le u < \infty$, $0 \le v < 2\pi$. Note that for a given interfocal distance d, the ellipse defined by constant u approaches a circle as u is increased. This is a desired property to have for the outer boundary,

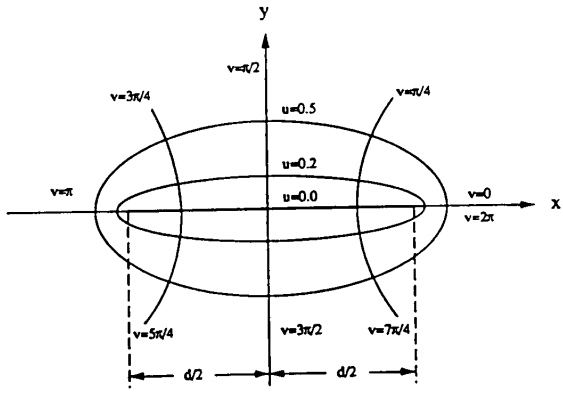

Figure 11.2.1 Elliptical coordinate system.

since the scattered field behaves like a cylindrical wave as the distance is increased. Also, when $d = 0$, the ellipse reduces to a circle.

By examining both the cylindrical and elliptical coordinate systems, we find in the limit as $d \to 0$ or $u \to \infty$ that v becomes ϕ. In the cylindrical coordinate system, r is the distance along a constant ϕ line. Therefore, we introduce an additional parameter n in the elliptical coordinate system, which is defined to be the arc length along a constant v curve.

$$n = \int_0^u \frac{d}{2}\sqrt{\cosh^2 u' - \cos^2 v}\, du' \tag{11.2.29}$$

Now, n becomes the radius when the ellipse approaches a circle, and $\hat{n}$ is the unit normal vector. Partial derivatives with respect to n and u are related by

$$\frac{\partial}{\partial n} = \hat{n} \cdot \nabla = \frac{2}{d[\cosh^2 u - \cos^2 v]^{1/2}} \frac{\partial}{\partial u} \tag{11.2.30}$$

Using (11.2.29) and (11.2.30), we convert (11.2.27) to

$$\frac{\partial^2}{\partial n^2} + \frac{2 \sinh u \cosh u}{d[\cosh^2 u - \cos^2 v]^{3/2}} \frac{\partial}{\partial n} + \frac{4}{d^2[\cosh^2 u - \cos^2 v]} \frac{\partial^2}{\partial v^2} + k^2 = 0 \tag{11.2.31}$$

The above expression reduces to the cylindrical wave equation when the ellipse approaches a circle.

In order to derive the absorbing boundary conditions for the elliptical boundary, we complete the square and proceed to the factorization.

By noticing that

$$\frac{\partial^2}{\partial n^2} + b\frac{\partial}{\partial n} = \left(\frac{\partial}{\partial n} + \frac{b}{2}\right)^2 - \frac{b^2}{4} - \frac{1}{2}\frac{\partial b}{\partial n} \tag{11.2.32}$$

where b is an arbitrary function of n, we rewrite (11.2.31) as

$$\left(\frac{\partial}{\partial n} + \frac{\sinh u \cosh u}{d[\cosh^2 u - \cos^2 v]^{3/2}}\right)^2 + \frac{4}{d^2[\cosh^2 u - \cos^2 v]}\frac{\partial^2}{\partial v^2} + k^2 - A = 0 \tag{11.2.33}$$

where

$$A = \frac{2}{d^2[\cosh^2 u - \cos^2 v]^3}\left(\sin^2 v(\sinh^2 u + \cosh^2 u) - \sinh^2 u\left(\frac{1}{2}\cosh^2 u + 1\right)\right) \tag{11.2.34}$$

Equation (11.2.33) is then factored into the following form:

$$\left(\frac{\partial}{\partial n} + \frac{\sinh u \cosh u}{d[\cosh^2 u - \cos^2 v]^{3/2}} + \lambda_+\right)\left(\frac{\partial}{\partial n} + \frac{\sinh u \cosh u}{d[\cosh^2 u - \cos^2 v]^{3/2}} - \lambda_-\right) = 0 \tag{11.2.35}$$

Then, following a similar approach as in the circular boundary case, we obtain

$$\lambda_+^{(1)} = \lambda_-^{(1)} = \lambda^{(1)} = ik\sqrt{1 + \frac{4}{(kd)^2[\cosh^2 u - \cos^2 v]}\frac{\partial^2}{\partial v^2} - \frac{A}{k^2}} \simeq ik\left(1 + \frac{2}{(kd)^2[\cosh^2 u - \cos^2 v]}\frac{\partial^2}{\partial v^2} - \frac{A}{2k^2}\right) \tag{11.2.36}$$

and

$$\lambda_+^{(0)} = \lambda_-^{(0)} = \lambda^{(0)} = -\frac{1}{2\lambda^{(1)}}\frac{\partial \lambda^{(1)}}{\partial n} = -\frac{1}{d\lambda^{(1)}[\cosh^2 u - \cos^2 v]^{1/2}}\frac{\partial \lambda^{(1)}}{\partial u} \tag{11.2.37}$$

Taking the leading order term from the $\lambda^{(1)}$ in the denominator, we obtain

$$\frac{\partial}{\partial n} = ik - \frac{\sinh u \cosh u}{d[\cosh^2 u - \cos^2 v]^{3/2}} + \frac{i2k}{(kd)^2[\cosh^2 u - \cos^2 v]} \cdot \left(1 + \frac{2 \sinh u \cosh u}{ikd[\cosh^2 u - \cos^2 v]^{3/2}}\right) \left(\frac{\sinh^4 u}{4[\cosh^2 u - \cos^2 v]^2} + \frac{\partial^2}{\partial v^2}\right) \tag{11.2.38}$$

Then, making an approximation similar to the one used in (11.2.26) gives

$$\frac{\partial}{\partial n} = ik - \frac{\sinh u \cosh u}{d[\cosh^2 u - \cosh^2 v]^{3/2}} + \frac{i2k}{(kd)^2[\cosh^2 u - \cos^2 v]} \cdot \frac{\frac{\sinh^4 u}{4[\cosh^2 u - \cos^2 v]^2} + \frac{\partial^2}{\partial v^2}}{1 - \frac{2 \sinh u \cosh u}{ikd[\cosh^2 u - \cos^2 v]^{3/2}}} \tag{11.2.39}$$

The above equation is the second-order absorbing boundary condition on elliptical outer boundaries. In arriving at (11.2.39), the higher-order terms of A are ignored. The higher-order terms are determined by the power of the product of either ($d \cosh u$) or ($d \sinh u$), since they measure the size of the ellipse as does r in the case of a circle. We note that when $d = 0$, (11.2.39) reduces to (11.2.10).

At this point, it is worthwhile to examine the "on surface radiation condition (OSRC)" [50] interpretation of (11.2.10). According to [50], the r in (11.2.10) is replaced by the radius of curvature (R) and $\partial^2/r^2 \partial\phi^2$ by $\partial^2/\partial s^2$ where s is the arc length. With these transformations, (11.2.10) becomes:

$$\frac{\partial}{\partial n} = ik - \frac{1}{2R} + \frac{i}{2k} \frac{\frac{\partial^2}{\partial s^2} + \frac{1}{4R^2}}{1 - \frac{1}{ikR}} \tag{11.2.40}$$

For the elliptical outer boundary,

$$R = \frac{d[\cosh^2 u - \cos^2 v]^{3/2}}{2 \cosh u \sinh u} \tag{11.2.41}$$

$$\frac{\partial^2}{\partial s^2} = \frac{4}{d^2[\cosh^2 u - \cos^2 v]} \frac{\partial^2}{\partial v^2} - \frac{2 \sin 2v}{d^2[\cosh^2 u - \cos^2 v]^2} \frac{\partial}{\partial v} \tag{11.2.42}$$

Then (11.2.40) becomes

$$\frac{\partial}{\partial n} = ik - \frac{\sinh u \cosh u}{d[\cosh^2 u - \cosh^2 v]^{3/2}} + \frac{i2k}{(kd)^2[\cosh^2 u - \cos^2 v]} \cdot \frac{\frac{\sinh^2 u \cosh^2 u}{4[\cosh^2 u - \cos^2 v]^2} + \frac{\partial^2}{\partial v^2}}{1 - \frac{2 \sinh u \cosh u}{ikd[\cosh^2 u - \cos^2 v]^{3/2}}} \quad (11.2.43)$$

by ignoring the term involving $\partial/\partial v$. Comparing (11.2.39) with (11.2.43), we note that the OSRC interpretation gives the same result up to the second order with the difference appearing only in the higher order terms.

c. Numerical Results and Discussions

The absorbing boundary conditions on circular outer boundaries have been studied and their effectiveness and accuracy have been demonstrated [9,30,33]. In this section, we focus on evaluating the absorbing boundary condition on elliptical outer boundaries. The control region approximation [9] with triangular grids is used to discretize Maxwell's equations in the frequency domain (finite-difference frequency-domain, or FD-FD) and the absorbing boundary condition (11.2.39) is imposed on the outer boundary. The bistatic and monostatic two-dimensional radar cross sections are calculated and compared to the results obtained using the method of moments.

The three geometries considered are a conducting ellipse with a major axis of 2.5λ, an aspect ratio of 0.1, and an interfocal distance of 4.97λ, as shown in Fig. 11.2.2, a conducting strip with 5λ width and a conducting "airfoil". The FD-FD results will be compared with the method of moments (MoM) results. In the MoM, the pulse basis and testing functions are employed with 240 divisions in those cases, resulting in a length on the order of 0.042λ for each division. The results will be presented in terms of two-dimensional RCS which is defined as

$$\sigma(\text{dBm}) = 10 \log \lim_{r \to \infty} 2\pi r \left| \frac{E_s}{E_i} \right|^2$$

and expressed as dBm (in dB after normalized by 1 meter). The frequency is assumed to be 300 MHz in all cases.

The effectiveness of the elliptical outer boundary is first demonstrated by calculating the FD-FD results with circular and elliptical

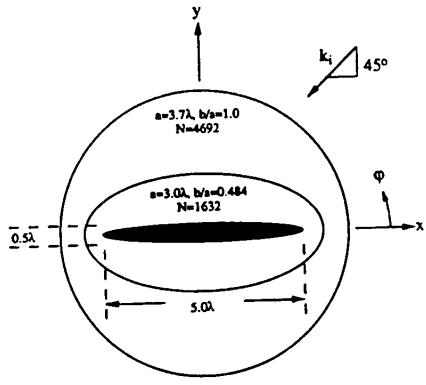

Figure 11.2.2 Circular and elliptical outer boundaries for a conducting ellipse: radius $r = 3.7\lambda$ for circular domain; $a = 3.0\lambda$ and $b/a = 0.484$ for elliptical domain.

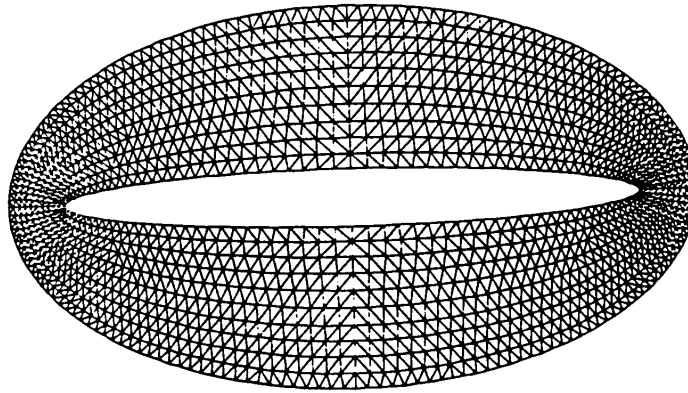

Figure 11.2.3 Triangular grid discretization of an elliptical computation domain with $a = 3.0\lambda$ and $b/a = 0.484$.

outer boundaries as shown in Fig. 11.2.2. The minimum separations from the elliptical and circular outer boundaries to the scatterer are 0.5λ and 1.2λ, respectively. Similar discretization is applied to both cases. A sample discretization for the elliptical boundary case is shown in Fig. 11.2.3. The number of unknowns for the elliptical and circular outer boundary cases are 1632 and 4692, respectively. The bistatic RCS as a function of scattering angle for an incidence angle of 45 degrees is shown in Fig. 11.2.4 and Fig. 11.2.5, for the electric field and magnetic field polarizations, respectively. As can be seen from the figures, the results obtained using the elliptical outer boundary seems to compare better with the MoM results than the circular boundary results.

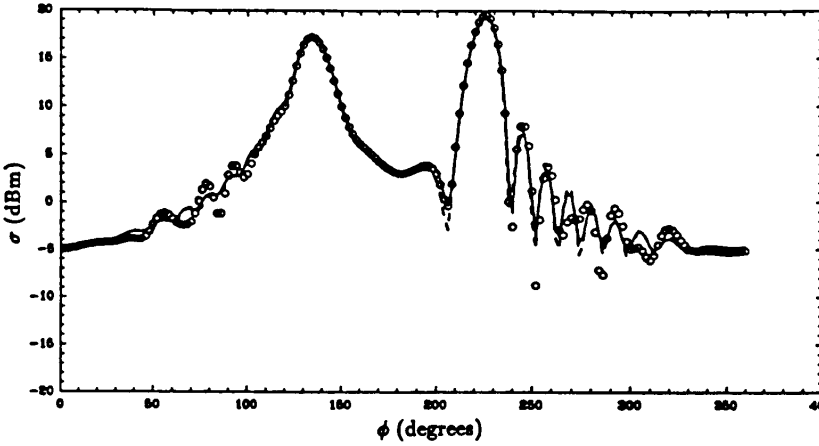

Figure 11.2.4 Bistatic RCS of a conducting ellipse with $a_o = 2.5\lambda$ and $b_o/a_o = 0.1$ at 300 MHz for electric field polarization for incidence angle of $\phi_i = 45°$. Solid curve: MoM; dashed curve: elliptical boundary with $a = 3.0\lambda$ and $b/a = 0.484$; circles: circular boundary with $r = 3.7\lambda$.

In order to simplify the comparison of the results, an *rms* error is defined as follows:

$$rms\text{dB} = \sqrt{\frac{\sum[\sigma(\text{dBm}) - \sigma_{MoM}(\text{dBm})]^2}{N}}$$

For the electric field polarization, the *rms* errors are found to be 0.58 dB and 1.0 dB for the elliptical and circular boundaries, respectively. For the magnetic field polarization, the *rms* errors are found to be 1.5 dB and 2.1 dB for the elliptical and circular boundaries, respectively. This clearly demonstrates that the number of unknowns can be reduced significantly, with the same level of accuracy, for elongated scatterers by using the elliptical outer boundaries with the absorbing boundary conditions given by (11.2.39).

In the case of the circular outer boundary, the radius of the circle is the only parameter which needs to be determined. In the case of the elliptical outer boundary, there are two free parameters: the interfocal distance and ellipticity, or equivalently, the major and minor axes a and b. The absorbing boundary condition is derived based on the

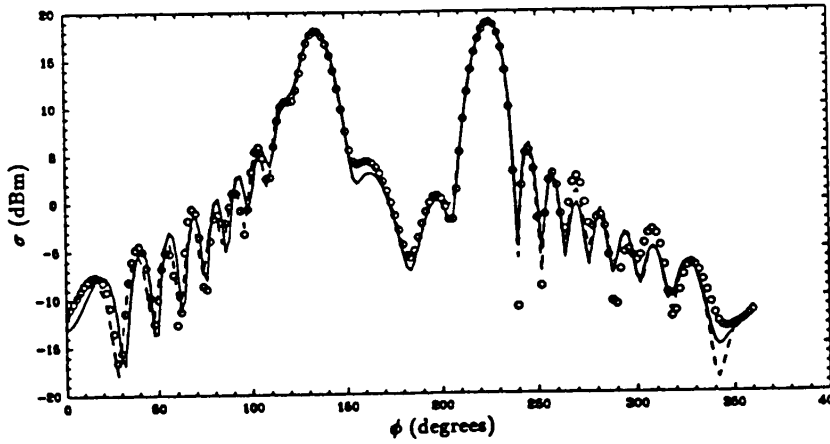

Figure 11.2.5 Bistatic RCS of a conducting ellipse with $a_o = 2.5\lambda$ and $b_o/a_o = 0.1$ at 300 MHz for magnetic field polarization for incidence angle of $\phi_i = 45°$. Solid curve: MoM; dashed curve: elliptical boundary with $a = 3.0\lambda$ and $b/a = 0.484$; circles: circular boundary with $r = 3.7\lambda$.

expansion of the scattered wave about the normal of the boundary. However, in general, it is difficult to know the optimum ellipticity due to the fact that one does not know the scattered wave front prior to solving the problem. In Figure 11.2.6, we show the same ellipse scatterer with two elliptical outer boundaries. We argue that the choice of the flat ellipse is not as good as the other ellipse, in spite of the fact that it is bigger. The main reason is that for the flat ellipse, the scattered wave will be incident at a steep angle to a portion of the ellipse near the end. To demonstrate this point, we compare the bistatic RCS of the conducting ellipse with two elliptical outer boundaries shown in Fig. 11.2.6. The angle of incidence is 45° and frequency is 300 MHz. Figure 11.2.7 and Fig. 11.2.8 show the bistatic RCS for electric and magnetic field polarizations, respectively. It is clear from the figures that the results for the smaller elliptical boundary compare better with the MoM results. The average *rms* differences for the flatter elliptical outer boundary is 1.90 dB compared to 1.04 dB for the case of the

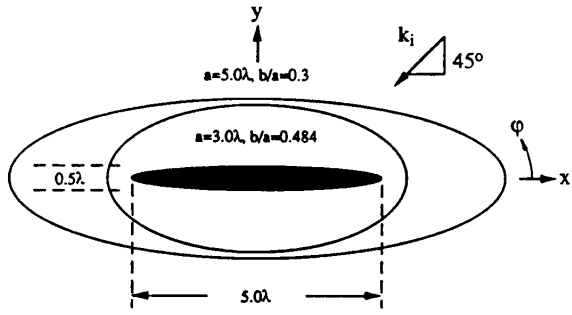

Figure 11.2.6 Two outer ellipses with different ellipticity.

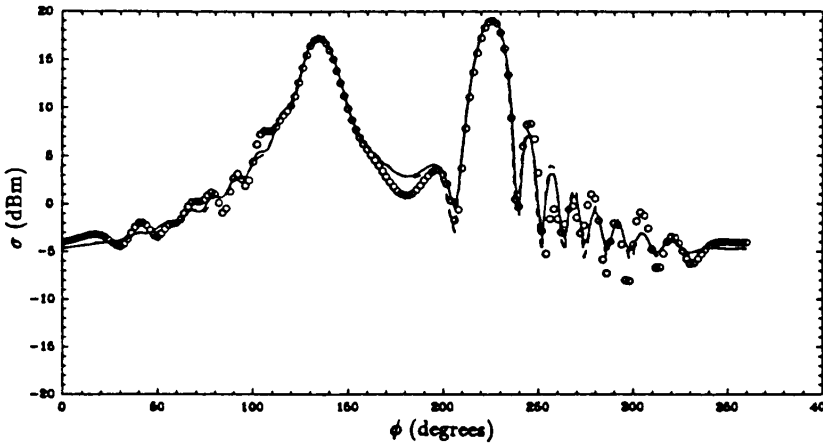

Figure 11.2.7 Bistatic RCS of a conducting ellipse with $a_o = 2.5\lambda$ and $b_o/a_o = 0.1$ at 300 MHz for electric field polarization for incidence angle of $\phi_i = 45°$. Solid curve: MoM; dashed curve: elliptical boundary with $a = 3.0\lambda$ and $b/a = 0.484$; circles: $a = 5.0\lambda$ and $b/a = 0.30$.

smaller elliptical boundary. Thus, the outer elliptical boundary should not be chosen to be more elongated than the scatterer.

In all of the above cases, the angle of the incident wave was fixed at $45°$. To further examine the absorbing boundary condition, the monostatic RCS is calculated as a function of angle of incidence for a 5λ wide conducting strip as shown in Fig. 11.2.9. The outer elliptical boundary used has the same shape as the one shown in Fig. 11.2.2 ($a = 3\lambda$ and $b/a = 0.484$). The monostatic RCS at 300 MHz is shown

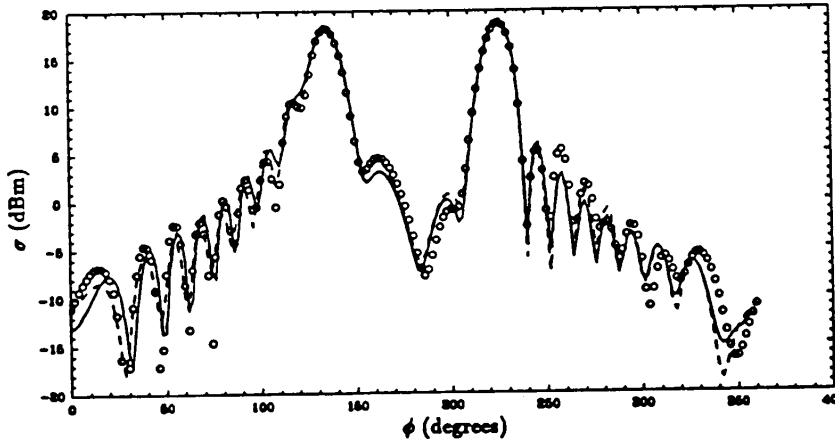

Figure 11.2.8 Bistatic RCS of a conducting ellipse with $a_o = 2.5\lambda$ and $b_o/a_o = 0.1$ at 300 MHz for magnetic field polarization for incidence angle of $\phi_i = 45^o$. Solid curve: MoM; dashed curve: elliptical boundary with $a = 3.0\lambda$ and $b/a = 0.484$; circles: $a = 5.0\lambda$ and $b/a = 0.30$.

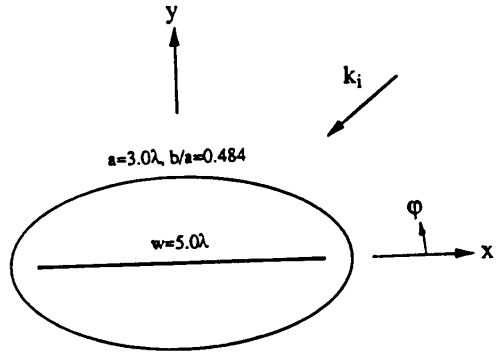

Figure 11.2.9 Geometrical description for FD-FD calculation of scattering by a 5λ conducting strip with an elliptical outer boundary ($a = 3.0\lambda$ and $b/a = 0.484$).

in Fig. 11.2.10 and Fig. 11.2.11 for electric field and magnetic field polarizations, respectively. Again, there is a good agreement between the MoM results and the FD-FD results obtained with the elliptical outer boundary. The average *rms* differences are 1.4 dB for the electric field and magnetic field polarizations.

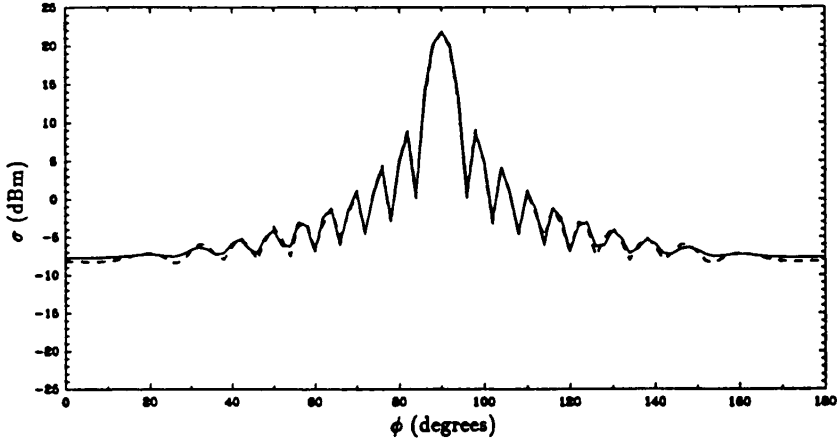

Figure 11.2.10 Monostatic RCS of 5λ conducting strip at 300 MHz for electrical field polarization. Solid curve: MoM; dashed curve: FD-FD with elliptical outer boundary.

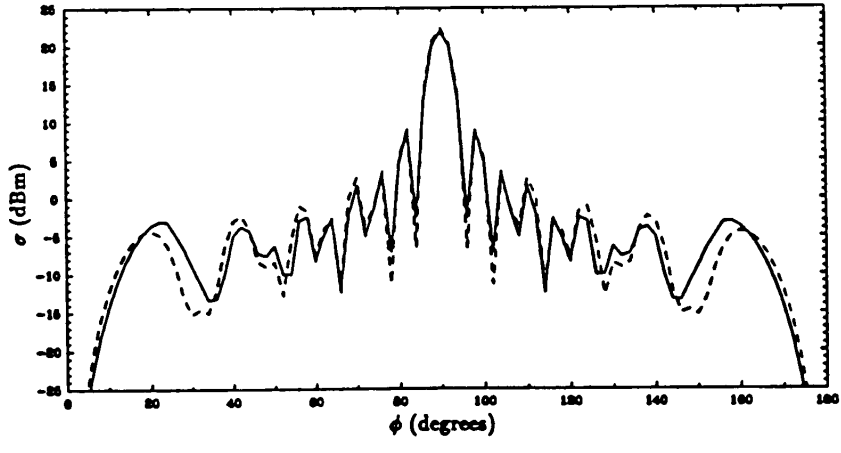

Figure 11.2.11 Monostatic RCS of 5λ conducting strip at 300 MHz for magnetic field polarization. Solid curve: MoM; dashed curve: FD-FD with elliptical outer boundary.

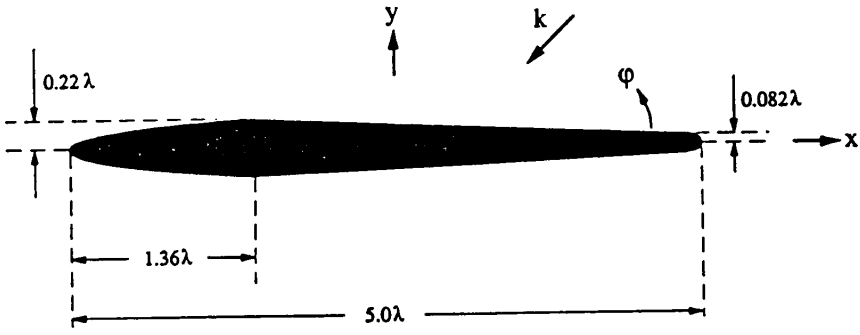

Figure 11.2.12 Geometrical description of an hypothetical "airfoil".

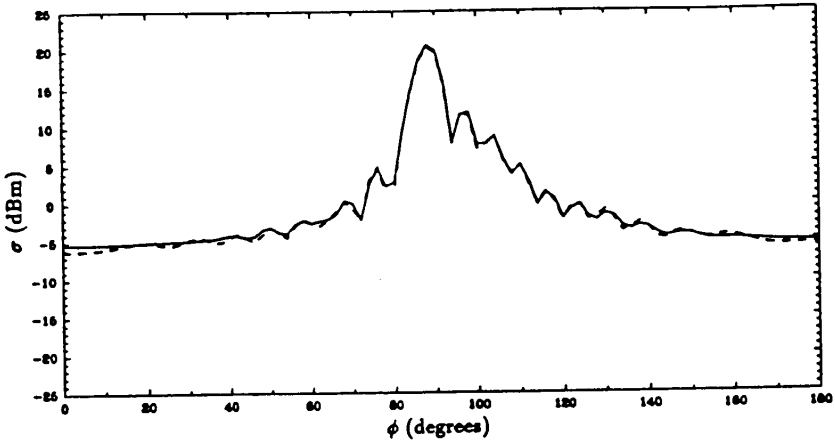

Figure 11.2.13 Monostatic RCS of a conducting "airfoil" at 300 MHz for electrical field polarization. Solid curve: MoM; dashed curve: FD-FD with elliptical outer boundary.

The last geometry to be analyzed is a hypothetical "airfoil" shown in Fig. 11.2.12. This geometry contains a portion of the ellipse analyzed previously, a half circle, and two straight sections. The same outer elliptical boundary as shown in Fig. 11.2.9 is used. Figure 11.2.13 and Fig. 11.2.14 show the monostatic RCS at 300 MHz for electric field and magnetic field polarizations, respectively. A good agreement between the MoM results and the FD-FD results is illustrated.

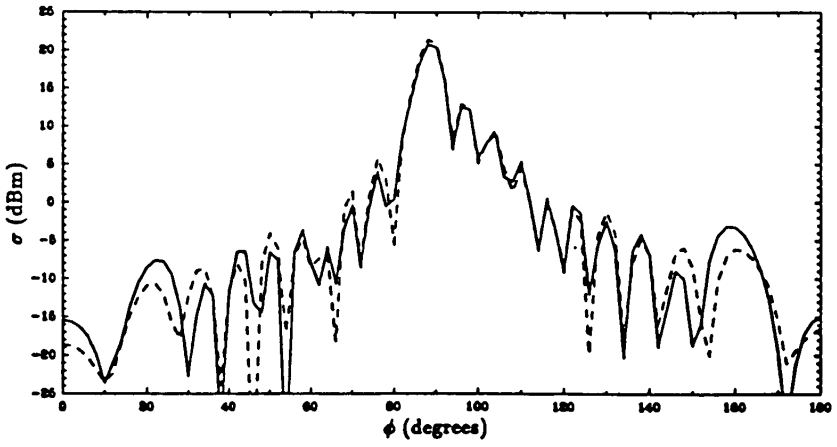

Figure 11.2.14 Monostatic RCS of 5λ conducting "airfoil" at 300 MHz for magnetic field polarization. Solid curve: MoM; dashed curve: FD-FD with elliptical outer boundary.

11.3 Finite-Difference Time-Domain Technique on Triangular Grids

In analyzing the problem of electromagnetic wave scattering from arbitrarily shaped scatterers (Fig. 11.3.1), the general procedure of the FD-TD technique involves approximating the Maxwell's equations using finite differences, imposing appropriate boundary conditions, and explicitly time-marching to obtain the direct time domain response. In order to apply the finite difference approximation to the Maxwell's equations, the electric and magnetic fields are discretized inside a finite computational domain. The discretization grids may be rectangular, triangular or other shapes. Nevertheless, the choice of the grid should enable accurate geometrical modeling of the scatterer.

For electromagnetic problems, rectangular grids are perhaps the most commonly used grids. The Yee's discretization scheme [1] of all field variables in space and time is employed with the rectangular grid, where the electric fields and the magnetic fields are temporally separated by a half a time step. In addition, they are spatially interlaced by half a grid cell. Based on this discretization scheme, a straightforward

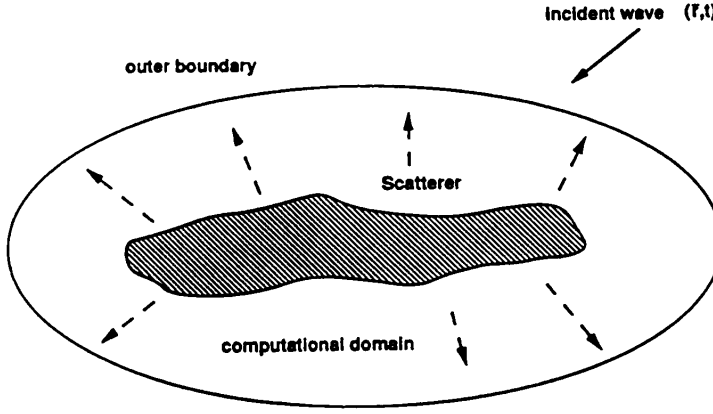

Figure 11.3.1 Configuration for electromagnetic scattering problems.

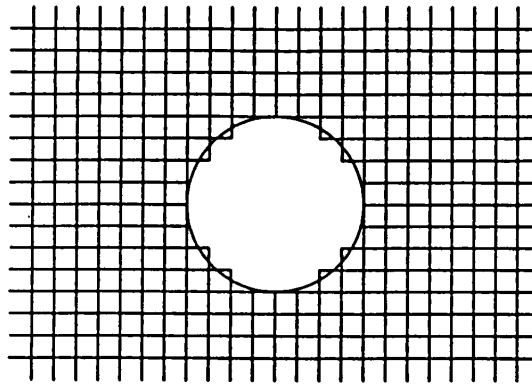

Figure 11.3.2 Rectangular grids and the staircase approximation of a conducting cylinder.

center differences in both space and time are applied to approximate the Maxwell's equations. The FD-TD algorithm based on the Yee's discretization scheme is very simple to implement. However, due to the fact that all grid cells are rectangular in shape, arbitrary geometries are approximated by staircases. Figure 11.3.2 shows a staircase approximation of a circular cylinder geometry. The staircase approximation may provide reasonably accurate electromagnetic model. In some situations, e.g., when strong surface waves are present, a very fine rectangular grids are needed to obtain accurate results for arbitrary geometries.

In order to avoid the staircase approximation for the arbitrary geometry, several discretization schemes have been proposed [4-7, 16,

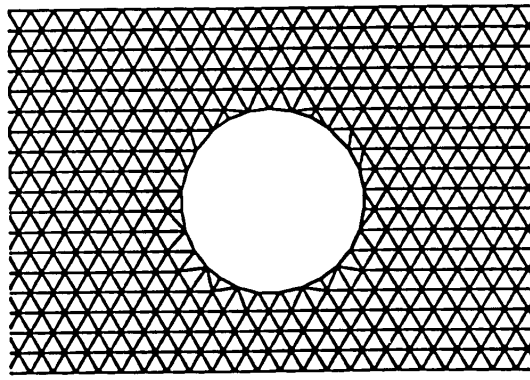

Figure 11.3.3 Triangular grids and modeling of a conducting cylinder.

17]. In [4], Holland suggested a generalized nonorthogonal grids and a corresponding discretization scheme. In his approach, a generalized coordinate system is created. The staircase approximation is eliminated by choosing the coordinate system to be naturally conforming to the geometry. However, the application to more general geometries appears cumbersome. In [7], a general finite difference scheme for nonorthogonal grid using the finite volume approach is discussed. An alternative in avoiding the staircase approximation is to use triangular grids [17]. The triangular grids provide flexibility in the accurate electromagnetic modeling of complex geometry. In applying the triangular grids, linear interpolations are used to describe the geometry surface. Figure 11.3.3 shows a geometry model of a coated cylinder using the triangular grids. The flexibility of the triangular grids can also be utilized to generate continuous outer boundaries, such as circular or elliptical boundaries. There are a number of discretization schemes associated with the triangular grids. The control region [9], defined by the Dirichlet tessellation, has been applied to two-dimensional (2D) frequency domain electromagnetic scattering problems. In this section, the control region approximation is extended to time domain electromagnetic scattering problems. The purpose is to develop a simple yet accurate algorithm for triangular grids to analyze time domain electromagnetic problems. In fact, the algorithm is basically a combination of the finite difference scheme on triangular grid and the control region approximation.

In the following subsections the discretization schemes for all field variables and the finite difference approximation of Maxwell's equations are discussed. Then, the implementation of the ABC on the cir-

cular and elliptical boundaries are discussed, and finally, the FD-TD algorithm is illustrated by calculating the time domain scattering problems with simple geometries.

a. Discretization on Triangular Grids

In the finite-difference time-domain algorithm, the discretization of the electric and magnetic fields are carried out in both time and space. The temporal discretization used is similar to that of Yee's scheme[1], where the electric and magnetic fields are interlaced in half a time step. The spatial discretization of fields are in triangular grids. Maxwell's equations are approximated using the finite difference approximation in conjunction with the control region approximation. To facilitate the discussion, a local coordinate system is defined (Fig. 11.3.4), where $\hat{s}$ and $\hat{n}$ are defined to be unit tangent and normal vectors along an arbitrary contour such that $\hat{n} \times \hat{s} = \hat{z}$. For 2D configuration, the problem can be divided into the electric field polarization and the magnetic field polarization cases. For electric field polarization, $\overline{E} = \hat{z}\,E$, Maxwell's equations are written as follow:

$$\nabla_T \times \eta_o (\hat{n} H_n + \hat{s} H_s) = \eta_o \sigma_e E_z + \hat{z}\,\epsilon_r \frac{\partial E_z}{c\,\partial t} \tag{11.3.1}$$

$$\frac{\partial E_z}{\partial n} = \sigma_m H_s + \mu_r \eta_o \frac{\partial H_s}{c\,\partial t} \tag{11.3.2}$$

$$\frac{\partial E_z}{\partial s} = -\sigma_m H_n - \mu_r \eta_o \frac{\partial H_n}{c\,\partial t} \tag{11.3.3}$$

For magnetic field polarization, $\overline{H} = \hat{z}\,H_z$, Maxwell's equations are written as follow:

$$\nabla_T \times (\hat{n} E_n + \hat{s} E_s) = -\sigma_m H_z - \hat{z}\,\mu_r \eta_o \frac{\partial H_z}{c\,\partial t} \tag{11.3.4}$$

$$\eta_o \frac{\partial H_z}{\partial n} = -\eta_o \sigma_e E_s - \epsilon_r \frac{\partial E_s}{c\,\partial t} \tag{11.3.5}$$

$$\eta_o \frac{\partial H_z}{\partial s} = \eta_o \sigma_e E_n + \epsilon_r \frac{\partial E_n}{c\,\partial t} \tag{11.3.6}$$

In the above equations, E_z, H_z, E_n, E_s, H_n, and H_s are total field quantities, and ϵ_r, μ_r, $\sigma_e\,(1/\mathrm{m}\Omega)$, $\sigma_m\,(\Omega/\mathrm{m})$, $\eta_o\,(\Omega)$, and c (m/s) are relative permittivity, relative permeability, electric conductivity,

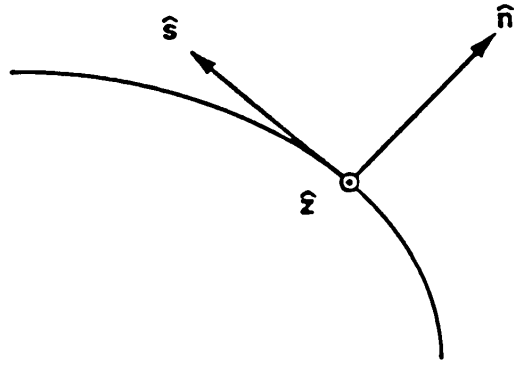

Figure 11.3.4 Local coordinate system.

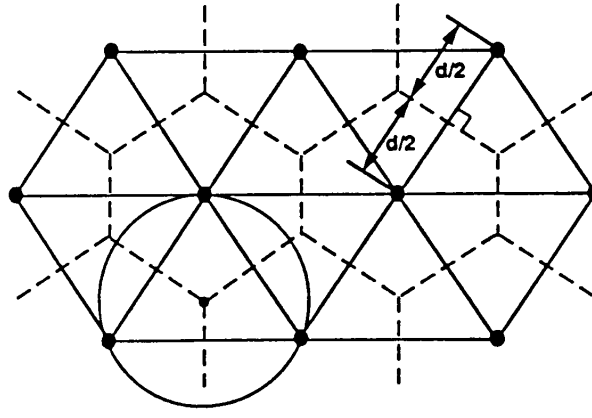

Figure 11.3.5 Topology of the Dirichlet and Delaunay tessellations.

magnetic conductivity, free space impedance, and speed of light in free space, respectively. The field quantities in the above equations can be broken up into the scattered and incident fields, where the incident field satisfies the free space Maxwell's equations. It turns out that FD-TD technique is simpler to implement if the total-scattered field technique based on [32] is employed.

In approximating the above equations, the control region approximation, which has been successfully applied to the frequency domain problems, is used. The control region approximation calls for Dirichlet and Delaunay tessellations, which is illustrated in Fig. 11.3.5. Delaunay tessellations are defined by the triangular grids. The Dirichlet tessellations are defined by polygons, which are orthogonal to the triangular grids. An important feature of this topology is that the edges of the

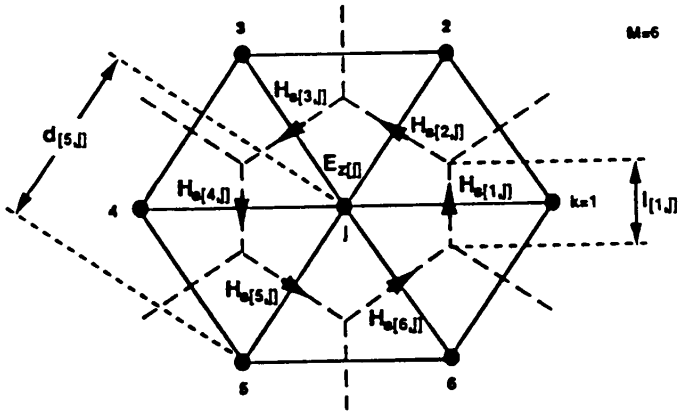

Figure 11.3.6 Field assignments on a Delaunay tessellation (electric field polarization).

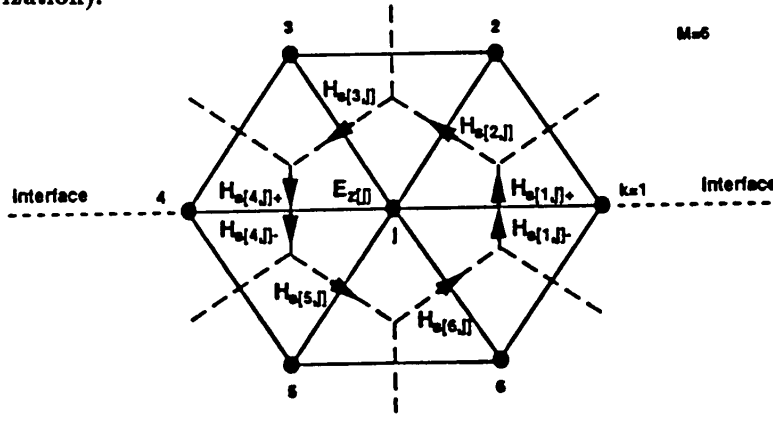

Figure 11.3.7 Field assignments on a Delaunay tesselation along an interface (electric field polarization).

Dirichlet tessellations are perpendicular bi-sectors of the corresponding triangular edge.

For electric field polarization, the FD-TD algorithm can be written in terms of E_z and H_s. Integrating (11.3.1) on a finite area and applying the Green's theorem, we obtain

$$\oint \eta_o H_s \, ds = \iint \left(\eta_o \sigma_e E_z + \epsilon_r \frac{\partial E_z}{c \, \partial t} \right) dA \qquad (11.3.7)$$

Since (11.3.7) and (11.3.2) only involve E_z and H_s and hence H_n is decoupled, we note that (11.3.3) can be discarded in the computation. To discretize these two equations, the control region defined by the Dirichlet tessellation is used. The field discretization in a control region

is shown in Fig. 11.3.6. The E_z are placed at nodes and H_s are placed along the Dirichlet edges. An unique orientation is assigned to each H_s, which is associated with two nodes. The convention of choosing the orientation is that the H_s is always counter clockwise with respect to the node with larger index. For total field node 'j' not lying on the interfaces and at time '$m-1/2$', (11.3.7) and (11.3.2) are approximated by,

$$\sum_{k=1}^{M} \eta_o H_{s[k,j]}^{m-1/2} l_{[k,j]} = \frac{\eta_o \sigma_e A}{2} (E_{z[j]}^m + E_{z[j]}^{m-1}) + \frac{\epsilon_r A}{c \Delta_t} (E_{z[j]}^m - E_{z[j]}^{m-1}) \tag{11.3.8}$$

$$\frac{1}{d_{[k,j]}} (E_{z[k]}^m - E_{z[j]}^m) = \frac{\sigma_m}{2} (H_{s[k,j]}^{m+1/2} + H_{s[k,j]}^{m-1/2}) + \frac{\mu_r \eta_o}{c \Delta_t} (H_{s[k,j]}^{m+1/2} - H_{s[k,j]}^{m-1/2}) \tag{11.3.9}$$

where A is the area of the control region, $l_{[k,j]}$ and $d_{[k,j]}$ are shown in Fig. 11.3.6. In deriving (11.3.8), the left-hand-side of (11.3.7) is approximated by summing contributions of H_s along the boundary of the control region 'j', where j is assumed to be bigger than k. If j is smaller than k, the corresponding contribution is negative. For terms involving conductivities, the time average approximation is employed. Finally, spatial and temporal derivatives are approximated by center differences. If node 'j' is in the free space, the terms involved conductivities vanish and relative permittivity and permeability are unity. Equation (11.3.8) is used to update electric fields, and the newly updated electric fields are used in (11.3.9) to update magnetic fields.

For total field node 'j' lying on the interfaces and at time '$m-1/2$', the discontinuity of normal magnetic fields must be considered. Since the normal magnetic flux density is continuous, the normal magnetic fields on both sides of the interface are related. The field assignments for this cases are shown in Fig. 11.3.7. In our implementation, the unknown normal magnetic fields are chosen to correspond to the field on the side with smaller relative permeability. Equation (11.3.7) and (11.3.2) are approximated using the identical expressions as in (11.3.8) and (11.3.9) except that the contributions along edges normal to the interface are split into two parts, one for each side of the interface.

For scattered field node ' j ' at time ' $m-1/2$ ', (11.3.7) and (11.3.2) are approximated as,

$$\sum_{k=1}^{M} \eta_o H^{m-1/2}_{s(s)[k,j]}\, l_{[k,j]} = \frac{\epsilon_r A}{c\,\Delta_t}\left(E^{m}_{z(s)[j]} - E^{m-1}_{z(s)[j]} \right) \tag{11.3.10}$$

$$\frac{1}{d_{[k,j]}}\left(E^{m}_{z(s)[k]} - E^{m}_{z(s)[j]} \right) = \frac{\mu_r \eta_o}{c\,\Delta_t}\left(H^{m+1/2}_{s(s)[k,j]} - H^{m-1/2}_{s(s)[k,j]} \right) \tag{11.3.11}$$

For magnetic field polarization, the FD-TD algorithm can be written in terms of E_s and H_z and is very similar to that of the electric field polarization case. Integrating (11.3.4) on a finite area and applying the Green's theorem, we obtain

$$\oint E_s\, ds = -\iint \left(\sigma_m H_z + \mu_r \eta_o \frac{\partial H_z}{c\,\partial t} \right) dA \tag{11.3.12}$$

Again, since (11.3.12) and (11.3.5) only involve H_z and E_s and hence E_n is decoupled, (11.3.6) is discarded in the computation. The field variable assignments are shown in Fig. 11.3.8, where H_z are placed at nodes and E_s are placed along the Dirichlet edges. The convention used in assigning orientation to H_s in the case of electric field polarization is used for assigning orientation of E_s.

For total field node ' j ' not lying on the interfaces and at time ' $m-1/2$ ', (11.3.12) and (11.3.5) are approximated by,

$$\sum_{k=1}^{M} E^{m-1/2}_{s[k,j]}\, l_{[k,j]} = -\frac{\sigma_m A}{2}\left(H^{m}_{z[j]} + H^{m-1}_{z[j]} \right) + \frac{\mu_r \eta_o A}{c\,\Delta_t}\left(H^{m}_{z[j]} - H^{m-1}_{z[j]} \right) \tag{11.3.13}$$

$$\frac{\eta_o}{d_{[k,j]}}\left(H^{m}_{z[k]} - H^{m}_{z[j]} \right) = -\frac{\sigma_m \eta_o}{2}\left(E^{m+1/2}_{s[k,j]} + E^{m-1/2}_{s[k,j]} \right) - \frac{\epsilon_r}{c\,\Delta_t}\left(E^{m+1/2}_{s[k,j]} - E^{m-1/2}_{s[k,j]} \right) \tag{11.3.14}$$

where A is the area of the control region, $l_{[k,j]}$ and $d_{[k,j]}$ are shown in Fig. 11.3.8. In deriving (11.3.13) and (11.3.14), the same techniques to derive (11.3.7) and (11.3.8) are used. If node ' j ' is in the free space,

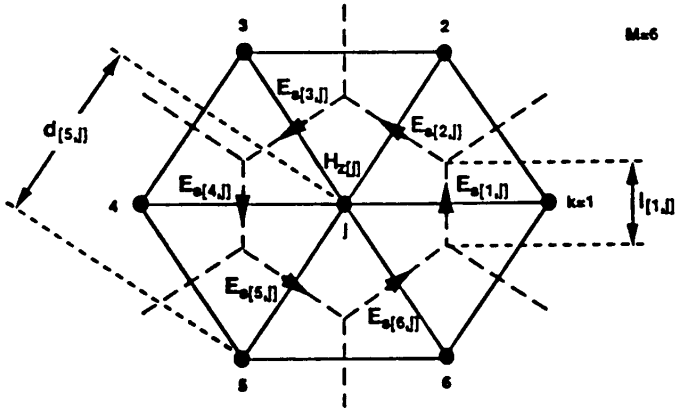

Figure 11.3.8 Field assignments on a Delaunay tessellation (magnetic field polarization).

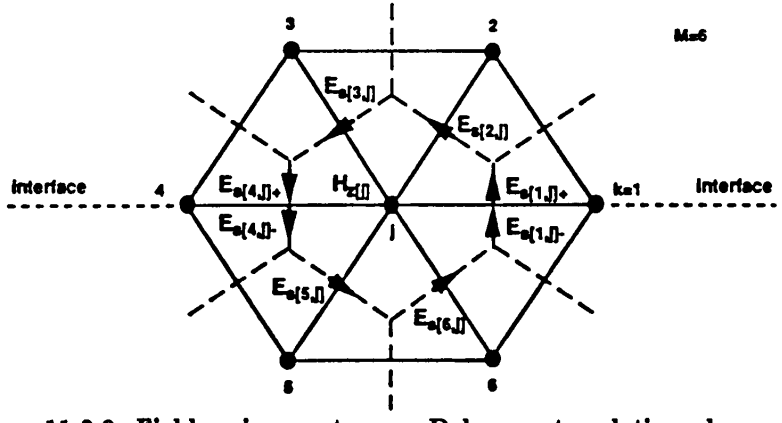

Figure 11.3.9 Field assignments on a Delaunay tesselation along an interface (magnetic field polarization).

the terms involving conductivities vanish and relative permittivity and permeability are unity. Equation (11.3.13) is used to update magnetic fields, and the newly updated magnetic fields are used in (11.3.14) to update electric fields.

For total field node 'j' lying on the interfaces and at time '$m - 1/2$', the discontinuity of normal electric fields must be considered. Since the normal electric displacement is continuous, the normal electric fields on both sides of the interface are related. The field assignments are shown in Fig. 11.3.9. For the FD-TD implementation, the unknown normal electric fields are chosen to correspond to the side having smaller relative permittivity. Equation (11.3.12) and (11.3.5) are approximated using the identical expressions as in (11.3.13) and

(11.3.14) except that the contributions along edges normal to the interface are split into two parts, one for each side of the interface.

For scattered field node 'j' at time '$m - 1/2$', (11.3.12) and (11.3.5) are approximated by,

$$\sum_{k=1}^{M} E^{m-1/2}_{s(s)[k,j]}\, l_{[k,j]} = -\frac{\mu_r\, \eta_o\, A}{c\, \Delta_t}\left(H^{m}_{z(s)[j]} - H^{m-1}_{z(s)[j]} \right) \qquad (11.3.15)$$

$$\frac{\eta_o}{d_{[k,j]}}\left(H^{m}_{z(s)[k]} - H^{m}_{z(s)[j]} \right) = -\frac{\epsilon_r}{c\, \Delta_t}\left(E^{m+1/2}_{s(s)[k,j]} - E^{m-1/2}_{s(s)[k,j]} \right) \qquad (11.3.16)$$

Equations (11.3.8) to (11.3.11) outline the two important steps of the FD-TD algorithm for the electric field polarization, and (11.3.13) to (11.3.16) outline the two important steps for the magnetic field polarization. The maximum dimension of a side of a triangular cell should be a small fraction of the minimum wavelength and Δ_t should be chosen such that the stability criterion is satisfied (Appendix). For equilateral triangular grids, the stability condition is

$$\Delta_t \leq \sqrt{\frac{2}{3}}\,\frac{h}{c} \qquad (11.3.17)$$

In the case of arbitrary triangular grids, a safety factor is needed.

Based on the above procedure, the evaluation of the fields at the outer boundary requires field information beyond the computational domain, which are not available. An exact boundary condition can be specified at the outer boundary of the computational domain. However, the field variables on the boundaries are coupled and the implementation of the boundary condition is numerically inefficient. An alternative is to impose the absorbing boundary conditions (ABC) [30,33].

b. Implementation of Absorbing Boundary Conditions

The absorbing boundary conditions (ABC) for two types of outer boundaries are used: circular and elliptical outer boundaries [30,33, 39]. For circular boundary, ABC can be expressed in operator form [30]

$$\left(\frac{\partial}{c\,\partial t} + \frac{1}{r} \right) \frac{\partial U}{\partial r} = -\frac{\partial^2 U}{c^2\,\partial t^2} - \frac{3}{2\,r\,c}\frac{\partial U}{\partial t} - \frac{3U}{8\,r^2} + \frac{1}{2\,r^2}\frac{\partial^2 U}{\partial \phi^2} \qquad (11.3.18)$$

This operator equation applies to the scattered fields at the boundary, i.e., $E_{z(s)}$ for electric field polarization and $H_{z(s)}$ for magnetic field

polarization. Figure 11.3.10 shows the field assignments at the boundary where U are either $E_{z(s)}$ or $H_{z(s)}$. The implementation of the ABC is basically the same as in Reference [32]. Along the dashed line in Fig. 11.3.10, at time step 'm', we have

$$\begin{aligned}\left(1+\frac{\Delta_r}{\Delta_t}+\frac{3\Delta_r}{4r_i}\right)u_{i1}^{m+1} &= \left(1-\frac{\Delta_r}{\Delta_t}-\frac{3\Delta_r}{4r_i}\right)u_{i0}^{m+1}\\ &+\left(1-\frac{\Delta_r}{\Delta_t}+\frac{3\Delta_r}{4r_i}\right)u_{i1}^{m-1}\\ &+\left(-1-\frac{\Delta_r}{\Delta_t}+\frac{3\Delta_r}{4r_i}\right)u_{i0}^{m-1}-\frac{2\Delta_t}{r_i}\left(u_{i1}^m-u_{i0}^m\right)\\ &+\left(\frac{2\Delta_r}{\Delta_t}-\frac{3\Delta_t\Delta_r}{8r_i^2}-\frac{\Delta_t\Delta_r}{\Delta_s^2}\right)\left(u_{i1}^m+u_{i0}^m\right)\\ &+\frac{\Delta_t\Delta_r}{2\Delta_s^2}\left(u_{jp1}^m+u_{jp0}^m+u_{jn1}^m+u_{jn0}^m\right) \qquad (11.3.19)\end{aligned}$$

where Δ_r, Δ_s, and r_j are shown in Fig. 11.3.10, and Δ_t is the time increment. In deriving (11.3.19), temporal and spatial center differences and time averaging techniques are used. In addition, the spacing between two boundary nodes are assumed to be constant.

For the elliptical outer boundary, the ABC in the frequency domain has been derived in the previous section [39]. The frequency domain result can be converted into the time domain result by applying the following transformation: $ik \rightarrow -\frac{\partial}{c\,\partial t}$. The time domain ABC of the elliptical boundary are expressed in the following operator equation:

$$\begin{aligned}\left(\frac{\partial}{c\partial t}+\frac{b}{a^2Z^{3/2}}\right)\frac{\partial}{\partial n} &= -\frac{\partial^2}{c^2\,\partial t^2}-\frac{3b}{2a^2Z^{3/2}}\frac{\partial}{c\,\partial t}\\ &+\frac{1}{2a^2Z}\frac{\partial^2}{\partial v^2}-\frac{b^2}{4a^4Z^3}\left(2-\frac{b^2}{2a^2}\right) \qquad (11.3.20)\end{aligned}$$

where

$$a=\frac{d}{2}\cosh u,\quad b=\frac{d}{2}\sinh u,\quad Z=1-\frac{\cos^2 v}{\cosh^2 u}$$

The same technique used in implementing the circular ABC can be utilized to implement the elliptical ABC.

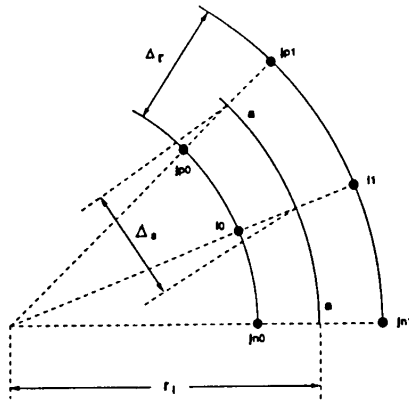

Figure 11.3.10 Field assignments on an outer boundary.

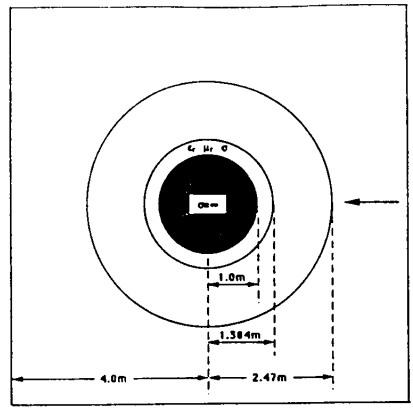

Figure 11.3.11 Coated conducting cylinder and computational domains.

c. Numerical Results

In this section, the FD-TD algorithm, outlined by (11.3.8) to (11.3.11) for electric field polarization and (11.3.13) to (11.3.16) for magnetic field polarization, and the implementation of the ABC on circular and elliptical boundaries are illustrated numerically. The scattering properties of two simple geometries are analyzed, circular cylinders and a strip. The FD-TD algorithm is applied to analyze conducting and coated conducting cylinders. The accuracy of geometry modeling using the triangular grid is evaluated and compared to that using the staircase approximation in the rectangular grid. The capability to treat

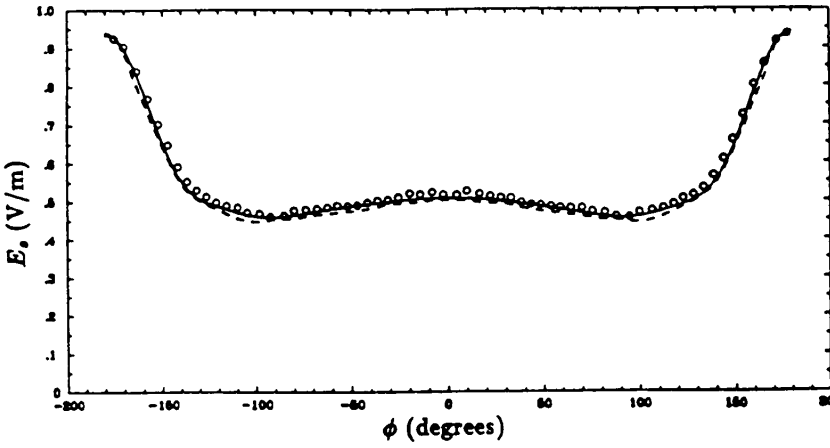

Figure 11.3.12 Amplitude of $E_{z(\phi)}$ along $r = 2.47$ m for electric field polarization. Coating: $\epsilon_r = 1.0$ and $\mu_r = 1.0$. Solid curve: eigen function expansion; dashed curve: triangular grid FD-TD; circles: rectangular grid FD-TD. Frequency: 150 MHz.

materials with electric and magnetic losses is analyzed. For scattering by a strip, the focus will be on the time domain ABC and transient analysis. The elliptical ABC is demonstrated to reduce the computational domain in certain cases. The transient response of the strip for a Gaussian incident pulse is also illustrated.

To examine the accuracy of the FD-TD algorithm, frequency domain quantities, such as field amplitudes at a particular frequency, are calculated using the FD-TD technique. These results are then compared with those obtained using frequency domain techniques. One way to obtain the frequency domain solutions via the FD-TD technique is to excite the scatterer with time dependent sinusoidal waves. The frequency domain solution is then extracted from the steady-state or the late time responses [13].

Figure 11.3.11 shows a configuration used in analyzing the scattering property of a two meter diameter conducting cylinder with 0.3 meter thick coated material. This geometry is analyzed using the rectangular grid FD-TD [1] and the triangular grid FD-TD. For triangular grid, the shape of the computational domain is a circle with a radius

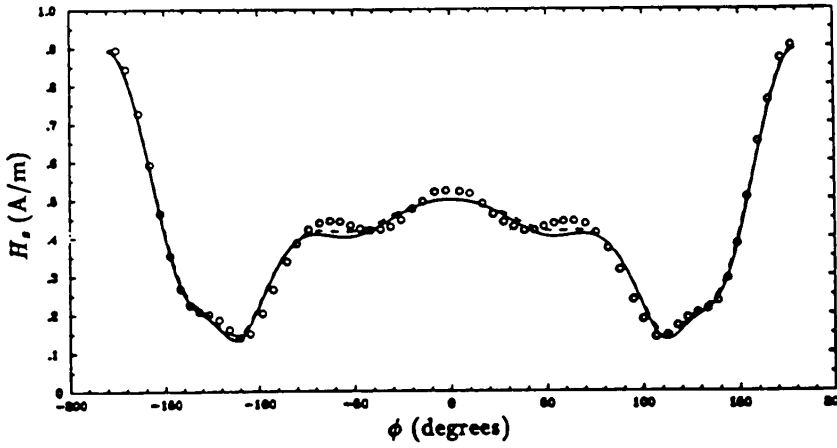

Figure 11.3.13 Amplitude of $H_{z(s)}$ along $r = 2.47$ m for magnetic field polarization. Coating: $\epsilon_r = 1.0$ and $\mu_r = 1.0$. Solid curve: eigen function expansion; dashed curve: triangular grid FD-TD; circles: rectangular grid FD-TD. Frequency: 150 MHz.

of 2.47 meter. For rectangular grid, a rectangular computational domain of 8 meter by 8 meter is chosen. The rectangular computational domain is considerably larger than the circular one to highlight the differences due to scatterer geometry modeling rather than the differences due to the ABC. The cylinder is excited by a sinusoidal plane wave at 150 MHz from $\phi = 0^o$. The steady-state amplitudes of the scattered fields at $r = 2.47$ meter circle are calculated using three techniques: the triangular grid FD-TD, the rectangular grid FD-TD, and the eigen function expansion method [63].

Figures 11.3.12 and 11.3.13 show the calculated $E_{z(s)}$ for electric field polarization and $H_{z(s)}$ for magnetic field polarization, respectively, for the case when the relative permittivity and permeability of the coating material are unity. The size of the triangular and rectangular grids are approximately $1/20\lambda$. The solid curves represent the results obtained using the eigen function expansion. The dashed curves are obtained using the triangular grid FD-TD, and the circles represent the results obtained using the rectangular grid FD-TD. In this case, both the rectangular and triangular grids provide accurate

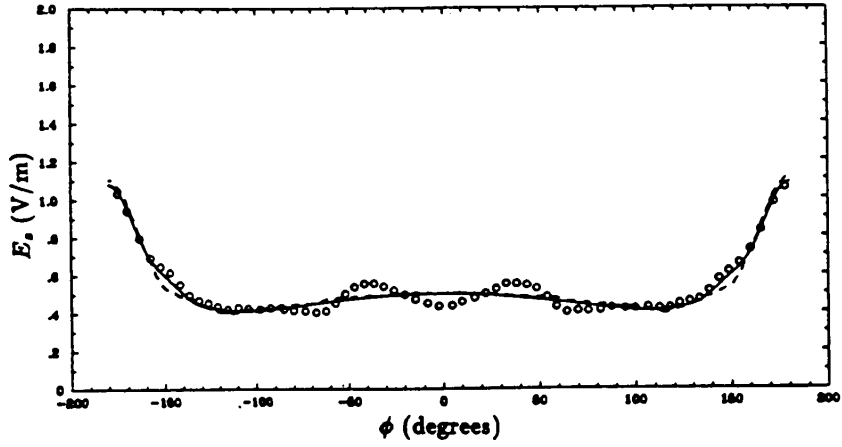

Figure 11.3.14 Amplitude of $E_{z(s)}$ along $r = 2.47$ m for electric field polarization. Coating: $\epsilon_r = 1.0$ and $\mu_r = 1.0$, Solid curve: eigen function expansion, dashed curve: triangular grid FD-TD; circles: rectangular grid FD-TD. Frequency: 300 MHz.

results, though the triangular grid provides a slightly more accurate results for magnetic field polarization case where the creeping waves are stronger.

The inaccuracy of the staircase geometry modeling in the rectangular grid becomes more noticeable when the grid size is increased with respect to the wavelength. This is illustrated by calculating the scattered field for the identical case at 300 MHz, which corresponds to the grid size of approximately $1/10\,\lambda$. The results are shown in Figs. 11.3.14 and 11.3.15 for electric and magnetic field polarization cases, respectively. It is shown that the triangular grid provides much more accurate results than the rectangular grid. This example suggests that the FD-TD based on the triangular grid can provide accurate solution with less number of discretization nodes than the rectangular grid.

The application of FD-TD technique for the coated conducting scatterer is illustrated by calculating the scattering characteristics of a conducting cylinder coated with dielectric material having $\epsilon_r = 3.0$ and $\sigma = 0.011/\mathrm{m}\Omega$, as shown in Fig. 11.3.11. The remaining parameters are the same as the previous case. For the incident plane wave

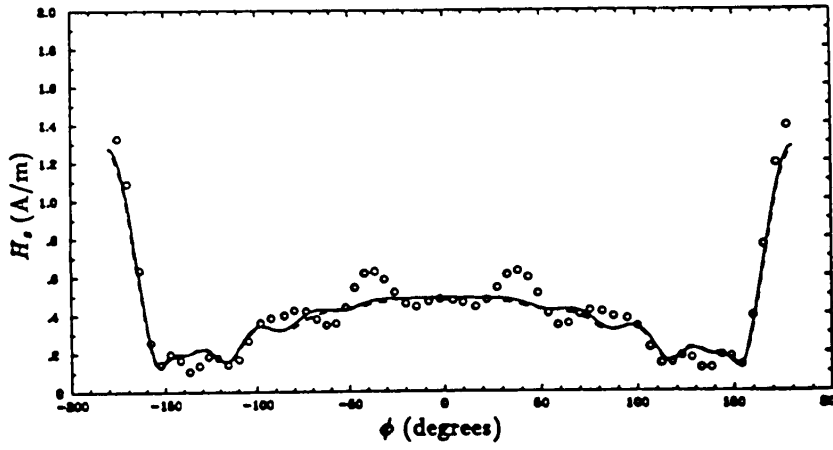

Figure 11.3.15 Amplitude of $H_{z(s)}$ along $r = 2.47$ m for magnetic field polarization. Coating: $\epsilon_r = 1.0$ and $\mu_r = 1.0$, Solid curve: eigen function expansion; dashed curve: triangular grid FD-TD; circles: rectangular grid FD-TD. Frequency: 300 MHz.

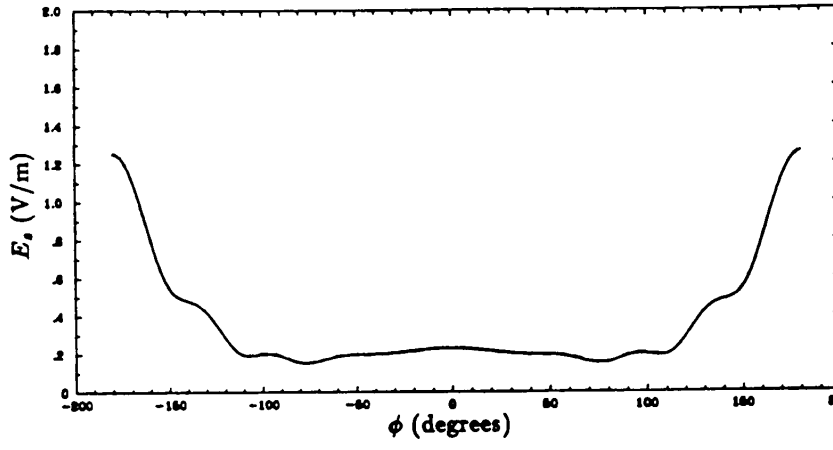

Figure 11.3.16 Amplitude of $E_{z(s)}$ along $r = 2.47$ m for electric field polarization. Coating: $\epsilon_r = 3.0$, $\mu_r = 1.0$ and $\sigma = 0.01/\text{m}\Omega$. Solid curve: eigen function expansion; dashed curve: triangular grid FD-TD. Frequency: 150 MHz.

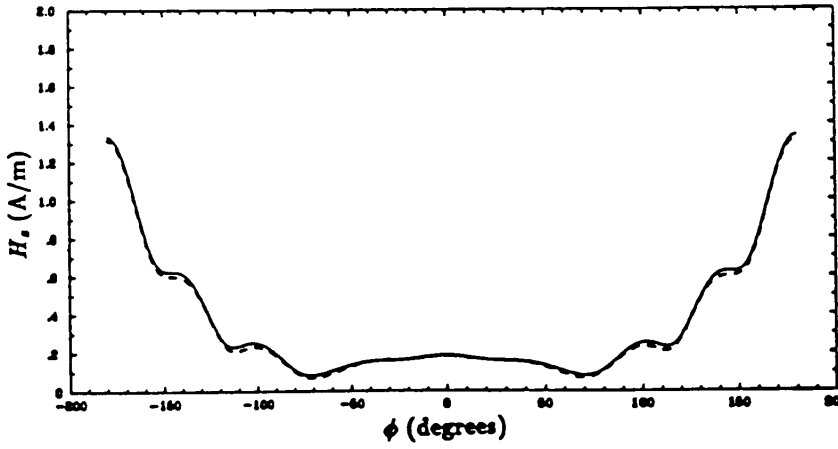

Figure 11.3.17 Amplitude of $H_{z(s)}$ along $r = 2.47$ m for magnetic field polarization. Coating: $\epsilon_r = 3.0$, $\mu_r = 1.0$ and $\sigma = 0.01/\text{m}\Omega$. Solid curve: eigen function expansion; dashed curve: triangular grid FD-TD. Frequency: 150 MHz.

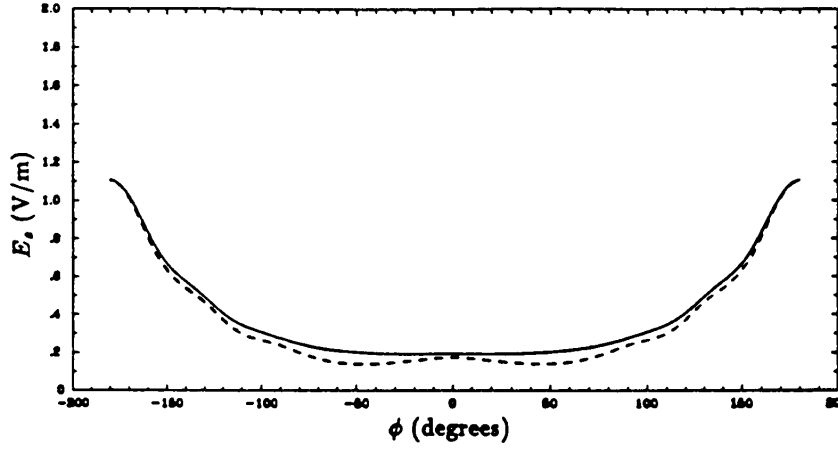

Figure 11.3.18 Amplitude of $E_{z(s)}$ along $r = 2.47$ m for electric field polarization, Coating: $\epsilon_r = 3.0$, $\mu_r = 3.0$ and $\sigma = 0.01/\text{m}\Omega$. Solid curve: eigen function expansion; dashed curve: triangular grid FD-TD. Frequency: 150 MHz.

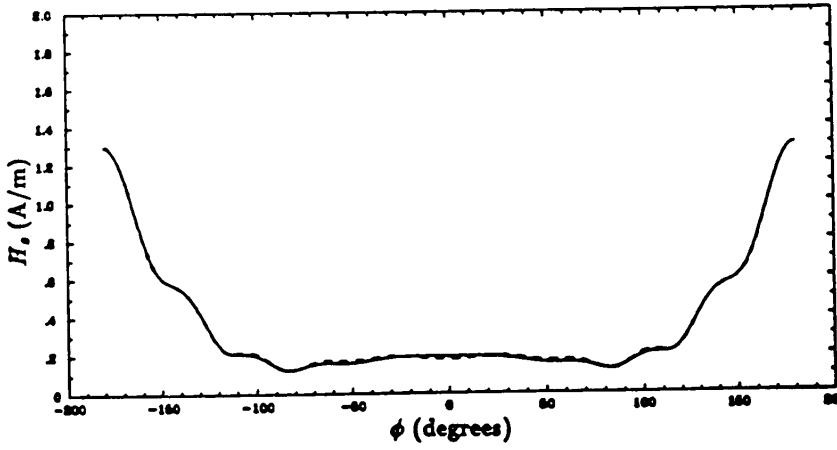

Figure 11.3.19 Amplitude of $H_{z(s)}$ along $r = 2.47$m for magnetic field polarization, Coating: $\epsilon_r = 3.0$, $\mu_r = 3.0$ and $\sigma = 0.01/\text{m}\Omega$. Solid curve: eigen function expansion, dashed curve: triangular grid FD-TD. Frequency: 150 MHz.

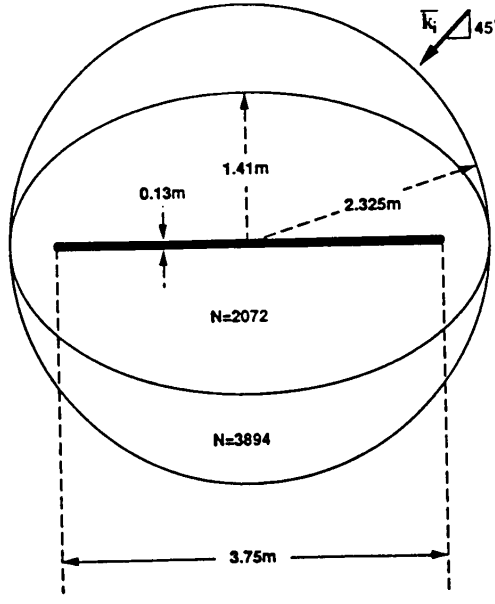

Figure 11.3.20 Conducting strip and computational domains. Grid size: 0.075 m.

at 150 MHz, the relative triangular grid size is approximately $1/14\,\lambda$ inside the coating material. The scattered fields along $r = 2.47$ meter radius are calculated for electric and magnetic field polarizations and shown in Fig. 11.3.16 and Fig. 11.3.17, respectively. The solid and dashed curves are the results obtained using the eigen function expansion and the FD-TD technique, respectively. As can be seen from the figures, there is an excellent agreement between two results.

In Figures 11.3.18 and 11.3.19, the results for the same cylinder with different coating material ($\epsilon_r = 3.0$ and $\sigma = 0.01/\mathrm{m}\Omega$, and $\mu_r = 3.0$) are presented. The size of the triangular grid and other parameters are the same as the last case. Again, there is a good agreement between the results obtained using the eigen function expansion and the triangular grid FD-TD technique. A slight discrepancy in the case of electric field polarization is primarily due to larger grid size inside the coating material (approximately $1/7\,\lambda$).

Previous numerical examples demonstrated the accuracy of the triangular grid FD-TD algorithm and the implementation of the time domain ABC on circular boundaries. For the circular computational domain, reflections generated at the boundary are very small when the second-order absorbing boundary condition is implemented. For elongated geometries, however, using the circular outer boundary may introduce unnecessarily large computational domains. In such cases, the elliptical outer boundary can be used to reduce the computational domain [39]. To illustrate this point, we consider a 5 meter wide, 0.13 meter thick strip with circular and elliptical computational domains, as shown in Fig. 11.3.20. The number of nodes for the circular and elliptical computational domains are 3894 and 2075, respectively. The ellipticity and size of the elliptical computational domain are selected by keeping the minimum separation from the ellipse to the strip to be the same distance as the minimum distance from the circle to the strip and setting the interfocal distance to be approximately 5 meters. A sinusoidal plane wave at 400 MHz is incident at $\phi = 45^o$. The relative grid size at this frequency is approximately 0.1 wavelength. The bistatic RCS results for the electric and magnetic field polarizations are shown in Figs. 11.3.21 and 11.3.22, respectively. The solid curves correspond to the results calculated using the method of moments and are taken as the reference in evaluating the accuracy of the FD-TD results. The triangular grid FD-TD algorithm is used to analyze the same problem, with dashed curves representing the results obtained using the ellip-

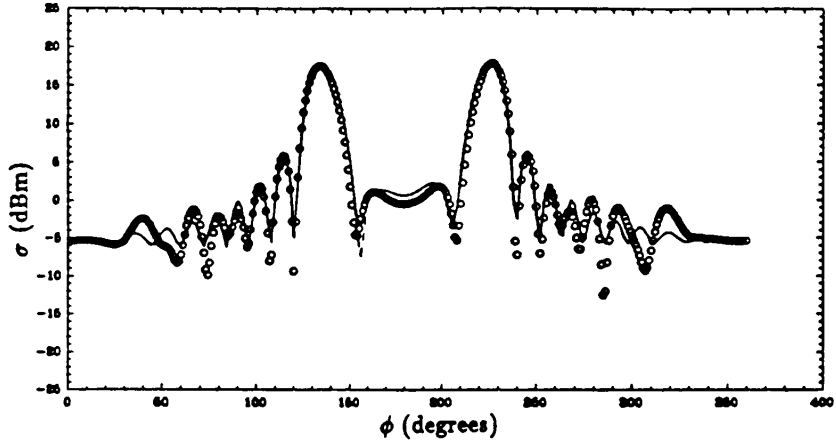

Figure 11.3.21 Bistatic scattering width of 5 m strip for electric field polarization. Frequency: 400 MHz; incident angle: 45°. Solid curve: method of moments, dashed curve: elliptical boundary; circles: circular boundary.

tical boundary and the circles representing results obtained using the circular boundary. As seen from Figs. 11.3.21 and 11.3.22, the results obtained using the elliptical boundary appear more accurate than the results obtained using the circular boundary. This is due to the fact that the elliptical boundary captures the scattered wave front from the edges better than the circular boundary for this configuration [39].

In all the previous examples, the steady-state (time-harmonic) results have been shown which demonstrated the stability and the accuracy of the FD-TD algorithm. In fact, the main advantage of the FD-TD technique is in its ability to handle time domain problems (e.g., transient analysis). This is demonstrated by calculating the time-domain scattered field from the strip shown in Fig. 11.3.20. The incident wave is a plane wave in space and Gaussian in time with the pulse width of 4.5 nano-second (ns). The incident pulse is propagating along $\phi = 45^o$. The size of the grids and other computational domain related parameters are the same as in the last case. The scattered fields at various time steps are shown in Fig. 11.3.23. The eight plots in Fig. 11.3.23 represent the transient magnetic field amplitudes on the entire computational domain at different time steps. The heights of the plots

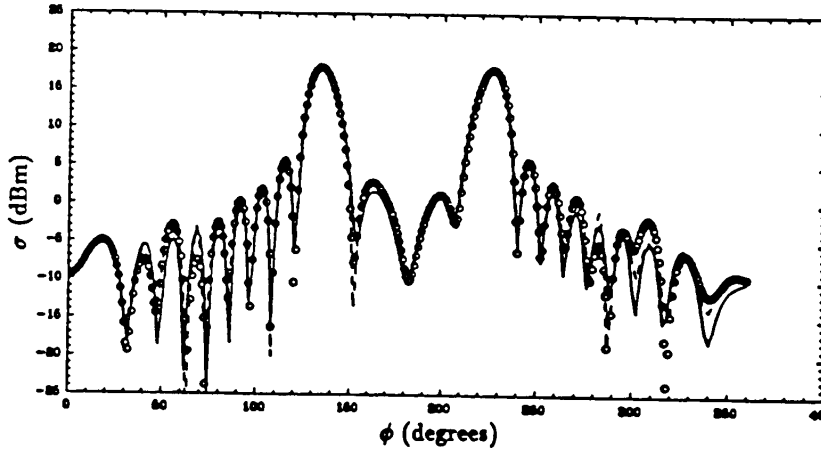

Figure 11.3.22 Bistatic scattering width of 5 m strip for magnetic field polarization. Frequency: 400 MHz; incident angle: 45°. Solid curve: method of moments, dashed curve: elliptical boundary; circles: circular boundary.

indicate the field amplitudes, which have been normalized in each plot. From these plots, the reflection, the edge diffraction, and the secondary diffraction between two edges are clearly shown and can be traced in time.

d. Appendix: Stability Criterion

In this appendix, the stability condition for the equilateral triangular grids is derived. The Dirichlet tessellation associated with the equilateral triangular grids in shown in Fig. 11.3.24. Focusing on the electric field polarization case (the same result can be derived for the magnetic field polarization case), we have the following equation in free space

$$\nabla^2 E_z - \frac{\partial^2 E_z}{\partial \tau^2} = 0$$

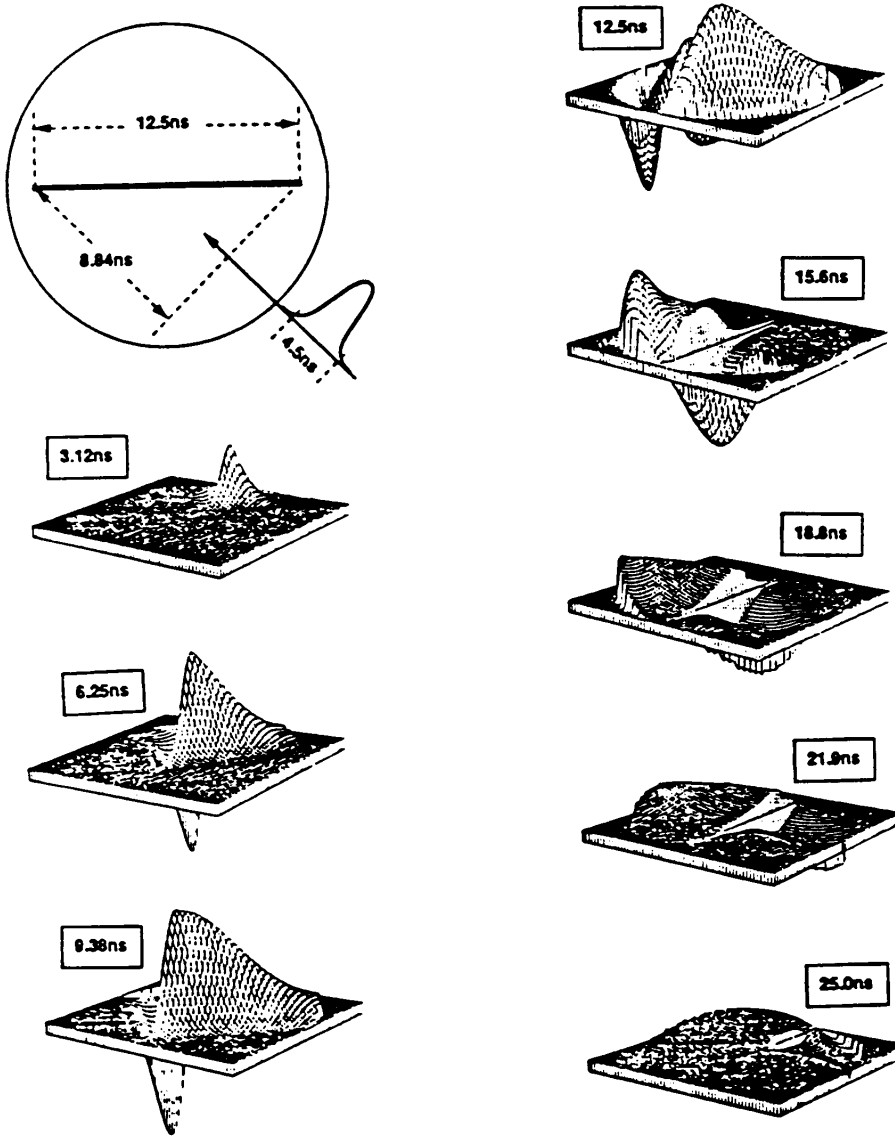

Figure 11.3.23 Gaussian pulse response of 5 m conducting strip for magnetic field polarization. Pulse width: 4.5 ns; incident angle: 45°. Frame 1: 3.12ns, frame 2: 6.25ns, frame 3: 9.38ns, frame 4: 12.5ns, frame 5: 15.6ns, frame 6: 18.8ns, frame 7: 21.9ns, and frame 8: 25.0ns.

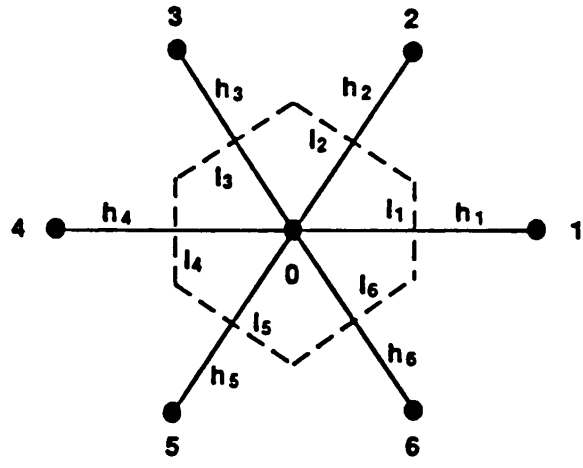

Figure 11.3.24 Control region for equilateral triangular grids.

where $\tau = ct$ is the normalized time. Integrating the above equation in the control region, we obtain

$$\oint \frac{\partial E_z}{\partial n}\, ds - \iint \frac{\partial^2 E_z}{\partial \tau^2}\, dA = 0$$

Applying the finite difference for normal derivatives and approximating the double integral by the value of the integrand at the node times the area of the control region, we obtain

$$\frac{l}{h} \sum_{1}^{6} \left(E^n_{z[i]} - E^n_{z[0]} \right) - \frac{A}{\Delta_\tau^2} \left(E^{n+1}_{z[0]} - 2\, E^n_{z[0]} + E^{n-1}_{z[0]} \right) = 0 \quad (A11.3.1)$$

Assume $E^n_{z[0]} = u^n e^{ik(x_o \cos\theta + y_o \sin\theta)}$, and $E^n_{z[i]} = u^n e^{ik(x_i \cos\theta + y_i \sin\theta)}$. We define the amplification factor to be

$$z = u^{n+1}/u^n$$

Substituting into (A11.3.1), we obtain

$$\frac{l}{h} z \sum_{1}^{6} \left(e^{ik((x_i - x_o)\cos\theta + (y_i - y_o)\sin\theta)} - 1 \right) - \frac{A}{\Delta_\tau^2} \left(z^2 - 2z + 1 \right) = 0$$

In order to have a stable algorithm, the maximum magnitude of z must not exceeds unity. Based on this condition, we find

$$\Delta_t \leq \sqrt{\frac{2}{3}}\frac{h}{c}$$

11.4 Application of Finite-Difference Time-Domain Techniques to Dispersive Materials

Because of the simplicity of the FD-TD algorithm, it has been used in analyzing electromagnetic problems involving complex structures, inhomogeneous materials, anisotropic materials, and time varying media. However, the application of the FD-TD technique to problems involving frequency dispersive materials has not been well explored.

Perhaps, the primary reason the FD-TD technique has not been widely applied to problems involving frequency dispersive material is the lack of an efficient time domain model. The FD-TD technique has been applied to problems in which the frequency dispersive material has a well-defined time domain model, such as plasma [20]. For general frequency dispersive materials, two approaches are usually taken. In the first approach, the relative permittivity, electric conductivity, relative permeability, and magnetic conductivity are approximated to be constant in the entire frequency range. This approach is only applicable to narrow frequency band problems. In the second approach, convolution integrals are employed

$$D(t) = \epsilon_0 \int_0^t d\tau\, \epsilon(t-\tau)E(\tau) \tag{11.4.1}$$

or

$$B(t) = \mu_0 \int_0^t d\tau\, \mu(t-\tau)H(\tau) \tag{11.4.2}$$

Since these convolutions are applied to every discretization point at every time step, this approach is very time consuming and requires a large memory. In addition, it is quite difficult to obtain $\epsilon(t)$ and $\mu(t)$ for general dispersive materials. An improved approach based on the convolution integrals is to model the time domain characteristic of the material using exponential functions [15]. This approach, again, requires $\epsilon(t)$ and $\mu(t)$.

In this section, a simple scheme to obtain efficient time domain models and a FD-TD algorithm for the frequency dispersive materials is discussed [59]. The technique does not require time domain convolution. The time domain models of the dispersive materials are written in the form of ordinary time differential equations. The FD-TD algorithm proposed is applicable to one-dimensional (1D), two-dimensional (2D), and three-dimensional (3D) problems. In the following subsections, we begin with an introduction to general frequency dispersive materials, which is followed by a discussion of the FD-TD algorithm, the required time domain models of the dispersive materials, and a discretization scheme for the 2D triangular grid configuration. Finally, the FD-TD technique is applied to 1D and 2D problems involving frequency dispersive materials.

a. Frequency Domain Models

In most of the practical situations, the dispersive characteristics of a material are described by a collection of discrete data points in a frequency band. The dispersive characteristic of the material may be governed by some complex physical phenomenon. Nevertheless, the mathematical description of the complex relative permittivity and permeability should obey the causality condition and at the same time provide a reasonable match with the discrete data.

The mathematical description of the causality condition is summarized in the Kramers-Krönig's relationships [60]. In the case of electric dispersion, the complex relative permittivity satisfies

$$\epsilon_R(\omega) - \epsilon_\infty = \frac{1}{\pi} \mathrm{PV} \int_{-\infty}^{\infty} d\omega' \frac{\epsilon_I(\omega')}{\omega' - \omega} \tag{11.4.3}$$

$$\epsilon_I(\omega) = -\frac{1}{\pi} \mathrm{PV} \int_{-\infty}^{\infty} d\omega' \frac{\epsilon_R(\omega') - \epsilon_\infty}{\omega' - \omega} \tag{11.4.4}$$

where

$$\epsilon(\omega) = \epsilon_R(\omega) + i\epsilon_I(\omega), \quad \epsilon_\infty = \epsilon(\infty) \tag{11.4.5}$$

The identical expressions are applied to the complex relative permeability in the case of magnetic dispersion.

To derive a mathematical model for the dispersive material, one may start with a set of laws which describe the physical process within the material. For the purpose of computation, however, one can select an appropriate mathematical expression which satisfies the causality

condition and reasonably describes the dispersive characteristic. There are a number of mathematical models which satisfy the causality condition. Three such models are the Debye model [60], the harmonic oscillator or the Lorentz model [61] in the case of electric dispersion, and the magnetic wall resonance model [62] in the case of magnetic dispersion. The molecular resonance model and the magnetic wall resonance model share a similar expression. For the Lorentz model and the magnetic wall resonance model, the following equations are used to describe the relative permittivity and permeability, respectively:

$$\epsilon(\omega) = 1 + \frac{\omega_{pE}^2}{\omega_{oE}^2 - \omega^2 - i2\rho_E\omega} \tag{11.4.6}$$

$$\mu(\omega) = 1 + \frac{\omega_{pM}^2}{\omega_{oM}^2 - \omega^2 - i2\rho_M\omega} \tag{11.4.7}$$

Figure 11.4.1 shows the complex relative permeability of a sample magnetic dispersive material. The 'o' and the '+' show the experimental data of the real and imaginary parts of the complex relative permeability of the material, respectively. The solid curves show the results calculated using (11.4.7) with the following parameters

$$\omega_{oM} = 2.0\pi(200\text{GHz}), \quad \rho_M\omega_{oM} = 20.0, \quad \omega_{pM}/\omega_{oM} = 1.73 \tag{11.4.8}$$

As seen from Fig. 11.4.1, (11.4.7) provides a reasonable match with the experimental data.

In the case of Debye model,

$$\epsilon(\omega) = \epsilon_\infty + \frac{\epsilon_s - \epsilon_\infty}{1 - i(\omega/\omega_0)} \tag{11.4.9}$$

This expression has been applied to model water in which case $\epsilon_\infty = 1.8$, $\epsilon_s = 81.0$, and $\omega_o = 2\pi(16.93\,\text{GHz})$ [15]. Figure 11.4.2 shows the real and imaginary parts of the relative permittivity for water.

b. Finite-Difference Time-Domain Algorithm

The conventional FD-TD algorithm for electromagnetic problems consists of two major steps [1,4,17]. In the first step, the previous time step magnetic field is used to update the electric field. In the second step, the newly updated electric field is used to calculate the magnetic

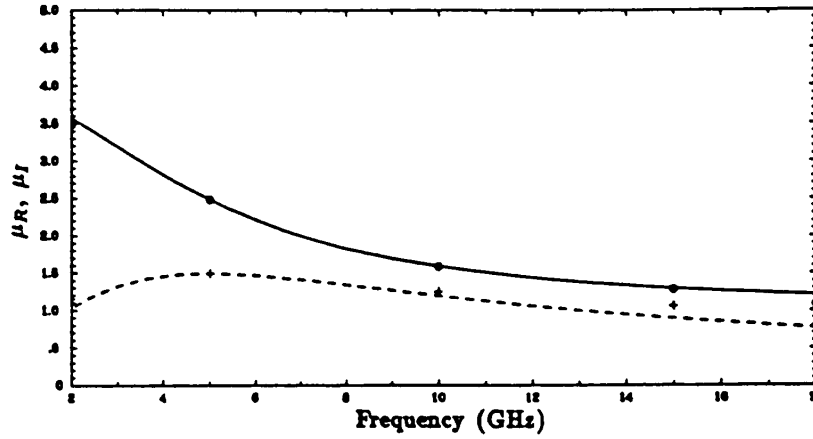

Figure 11.4.1 Relative permeability of a sample dispersive material with $\epsilon_R = 13.2$, and $\epsilon_I = 0.0$.'o': experimental real part; '+': experimental imaginary part;solid curve: calculated real part; dashed curve: calculated imaginary part.

field. These two steps may be swapped. In order to account for the dispersive characteristic, the two step FD-TD algorithm is expanded into a four step procedure. The additional steps are designed to relate $\overline{E}$ to $\overline{D}$ and $\overline{H}$ to $\overline{B}$.

For the reason of simplicity, the following normalized field variables are defined:

$$\overline{d} = \overline{D}/\epsilon_0, \quad \overline{e} = \overline{E}, \quad \overline{b} = \eta_0 \overline{B}/\mu_0, \quad \overline{h} = \eta_0 \overline{H} \tag{11.4.10}$$

In addition, the normalized time, $\tau = c_0 t$, is also defined. In Equation (11.4.10), ϵ_o, μ_o and η_o are the free space permittivity, permeability and impedance, respectively. With this normalized field quantities, the FD-TD algorithm is

$$\nabla \times \overline{h} = \frac{\partial \overline{d}}{\partial \tau} \tag{11.4.11a}$$

$$\overline{d} \rightarrow \overline{e} \tag{11.4.11b}$$

$$\nabla \times \overline{e} = -\frac{\partial \overline{b}}{\partial \tau} \tag{11.4.11c}$$

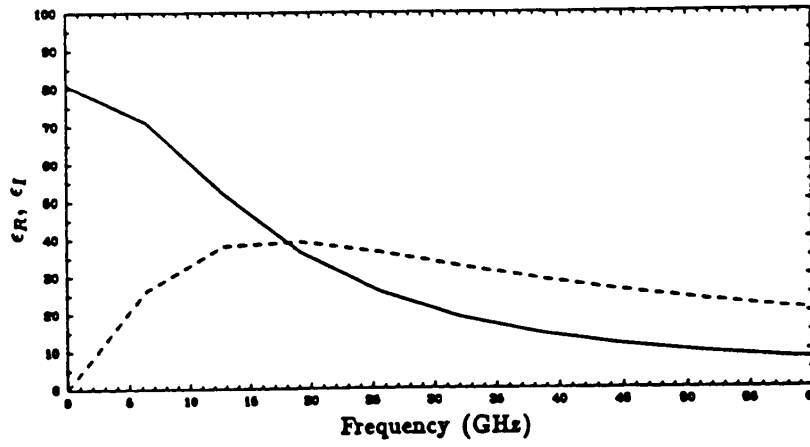

Figure 11.4.2 Relative permittivity of water. Solid curve: real part; dashed curve: imaginary part.

$$\overline{b} \rightarrow \overline{h} \tag{11.4.11d}$$

Steps 1 and 3 are almost identical to the conventional algorithm except that the variables $\overline{d}$ and $\overline{b}$ are introduced. To complete the algorithm, steps 2 and 4 require time domain models to describe the dispersive nature of the material.

The procedure to derive the appropriate time domain model is the same for electric and magnetic dispersive materials. Focusing on the electric dispersion,

$$\overline{d}(\omega) = \epsilon(\omega)\overline{e}(\omega), \tag{11.4.12}$$

where $\epsilon(\omega)$ may be obtained by selecting an appropriate model, such as (11.4.6) and (11.4.9), with parameters obtained by curve-fitting the experimental data. As suggested by (11.4.12), an obvious time domain model is the convolution which is inefficient. Instead, the following substitution

$$\frac{\partial}{\partial \tau} = -i\omega/c_0 \tag{11.4.13}$$

is made in (11.4.12). For the frequency domain model in (11.4.6), the

substitution leads to the following time domain model

$$\left(\frac{\partial^2}{\partial\tau^2} + 2\rho'\frac{\partial}{\partial\tau} + \omega_0'^2\right) d(\tau) = \left(\frac{\partial^2}{\partial\tau^2} + 2\rho'\frac{\partial}{\partial\tau} + \omega_0'^2 + \omega_p'^2\right) e(\tau) \tag{11.4.14}$$

where

$$\rho' = \rho_E/c, \quad \omega_0' = \omega_{0E}/c, \quad \omega_p' = \omega_{pE}/c \tag{11.4.15}$$

With the same substitution, the time domain model corresponding to (11.4.9) is

$$\left(\frac{1}{\omega_0'}\frac{\partial}{\partial\tau} + 1\right) d(\tau) = \left(\frac{\epsilon_\infty}{\omega_0'}\frac{\partial}{\partial\tau} + \epsilon_s\right) e(\tau) \tag{11.4.16}$$

These time domain models can be easily discretized. Since the time domain models, such as (11.4.14) and (11.4.16), are written as the ordinary time differential equations, the four step algorithm and its discretization schemes are applicable to 1D, 2D and 3D problems.

c. Discretization

There are a number of schemes available for discretizing the FD-TD algorithm for frequency dispersive material discussed in previous section. In fact most of the existing schemes, for example [1,16], can be easily integrated into the algorithm with little alteration. In this section, a discretization scheme based on triangular grid [16] is discussed. It should be straightforward to generalize to 3D configuration or other discretization schemes.

The time domain discretization of field variables is carried out in the temporal interlace manner. That is $d(\tau)$ and $e(\tau)$ are in integer time:

$$d^n, \quad e^n \tag{11.4.17}$$

and $b(\tau)$ and $h(\tau)$ are in half-integer time:

$$b^{n+1/2}, \quad h^{n+1/2} \tag{11.4.18}$$

This procedure is identical to those in [1,16], and the time marching is in the leap-frog manner. With this time arrangement, the time derivatives in steps 1 and 3 of (11.4.11) can be discretized using the center difference.

The discretization for steps 2 and 4 of (11.4.11) may be carried out using various methods available for ordinary differential equations. Using center difference in time, (11.4.6) can be discretized and rearranged to:

$$e^{n+1} = d^{n+1} + \frac{\Delta_\tau^2 \omega_0'^2 - 2}{1 + \Delta_\tau \rho'}(d^n - e^n) - \frac{\Delta_\tau^2 \omega_p'^2}{1 + \Delta_\tau \rho'} e^n + \frac{1 - \Delta_\tau \rho'}{1 + \Delta_\tau \rho'}(d^{n-1} - e^{n-1}) \quad (11.4.19)$$

As seen from (11.4.19), numerical treatment of the dispersive material modeled by (11.4.6) requires three levels of previous time information. Similarly, (11.4.16) can be discretized and rearranged to:

$$e^{n+1} = \frac{(\frac{1}{\omega_0'\Delta_\tau} + \frac{1}{2})d^{n+1} + (\frac{1}{2} - \frac{1}{\omega_0'\Delta_\tau})d^n + (\frac{\epsilon_\infty}{\omega_0'\Delta_\tau} - \frac{\epsilon_s}{2})e^n}{\frac{\epsilon_\infty}{\omega_0'\Delta_\tau} + \frac{\epsilon_s}{2}} \quad (11.4.20)$$

Due to the fact that the time domain model involves only the first order time derivative, the corresponding numerical treatment requires two levels of previous time information.

The spatial discretization refers to the discretization in steps 1 and 3 of the FD-TD algorithm in the previous section. For 2D triangular grid, the discretization is identical to the procedure described in Section 11.3 [16], except on the interface.

Maxwell's equations, written in terms of the normalized variables, for electric field polarization, are

$$\nabla_T \times (\hat{n} h_n + \hat{s} h_s) = \hat{z} \frac{\partial d_z}{\partial \tau} \quad (11.4.21)$$

$$\frac{\partial e_z}{\partial n} = \frac{\partial b_s}{\partial \tau} \quad (11.4.22)$$

$$\frac{\partial e_z}{\partial s} = -\frac{\partial b_n}{\partial \tau} \quad (11.4.23)$$

The relationship from $\bar{d}$ to $\bar{e}$ and $\bar{b}$ to $\bar{h}$ are given by the time domain models of the dispersive materials. Applying an area integral and Green's theorem to (11.4.21), b_n and h_n are decoupled from other field variables and the following equations are obtained:

$$\oint h_s \, dl = \iint \frac{\partial d_z}{\partial \tau} \, dA \quad (11.4.24)$$

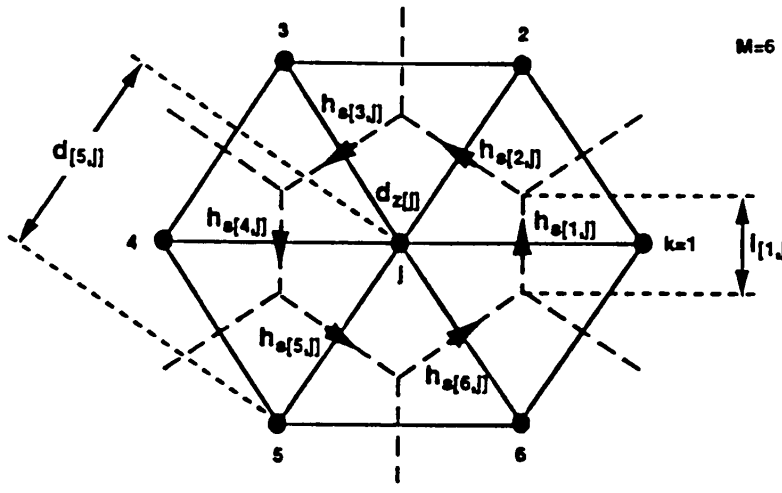

Figure 11.4.3 Field locations in a control region for electric field polarization.

$$\frac{\partial e_z}{\partial n} = \frac{\partial b_s}{\partial \tau} \tag{11.4.25}$$

These are the two equations corresponding to steps 1 and 3 in the FD-TD algorithm. Figure 11.4.3 shows the field locations in the control region. $\bar{e}$ and $\bar{d}$ are at the same location, and, similarly, $\bar{h}$ and $\bar{b}$ are at the same location. Equation (11.4.24) and (11.4.25) are discretized as follow:

$$\sum_{k=1}^{M} h_{s[k,j]}^{m-1/2} \, l_{[k,j]} = \frac{A}{\Delta_\tau} \left(d_{z[j]}^{m} - d_{z[j]}^{m-1} \right) \tag{11.4.26}$$

$$\frac{1}{d_{[k,j]}} \left(e_{z[k]}^{m} - e_{z[j]}^{m} \right) = \frac{1}{\Delta_\tau} \left(b_{s[k,j]}^{m+1/2} - b_{s[k,j]}^{m-1/2} \right) \tag{11.4.27}$$

where A is the area of the control region, Δ_τ is the normalized time step, and d is the separation between two nodes. The boundary conditions at perfectly conducting surfaces can be easily satisfied with this scheme. At the dispersive medium interface, however, a caution must be taken. Since both e_z and d_z are placed at the interface, the continuity of electric field is satisfied. The d_z at the interface is split to

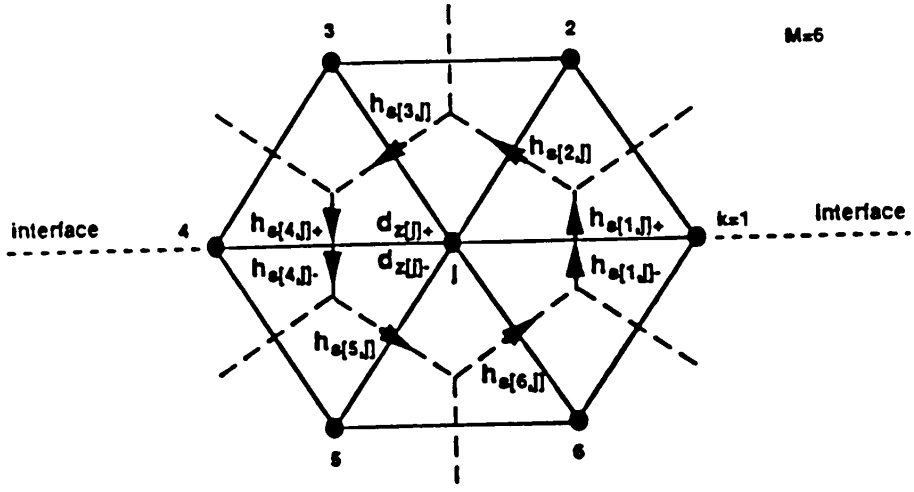

Figure 11.4.4 Field locations on the interface for electric field polarization.

the value just inside the interface (d_{z+}) and the value just outside the interface (d_{z-}). The continuity of normal magnetic flux density is satisfied due to the fact that b_s is normal to the interface. Different values of magnetic field are assigned at the interface; h_{s+} is the magnetic field value just inside the interface and h_{s-} is the magnetic field value just outside the interface. Figure 11.4.4 shows the field location assignment at the interface. With the above field location assignment, the discretization of (11.4.24) and (11.4.25) are

$$\sum_{k=1}^{M} h_{s\pm[k,j]}^{m-1/2}\, l_{[k,j]\pm} = \frac{A_+}{\Delta_\tau}\left(d_{z[j]+}^{m} - d_{z[j]+}^{m-1} \right) + \frac{A_-}{\Delta_\tau}\left(d_{z[j]-}^{m} - d_{z[j]-}^{m-1} \right) \tag{11.4.28}$$

$$\frac{1}{d_{[k,j]}}\left(e_{z[k]}^{m} - e_{z[j]}^{m} \right) = \frac{1}{\Delta_\tau}\left(b_{s[k,j]}^{m+1/2} - b_{s[k,j]}^{m-1/2} \right) \tag{11.4.29}$$

The relationship between two unknowns ($d_{z[j]+}$ and $d_{z[j]-}$) in (11.4.28) can be obtained by utilizing material models on both sides of the interface and the continuity of tangential electric field. The material models on both sides of the interface are also used to calculate h_{s+} and h_{s-}, once b_s is found from (11.4.29).

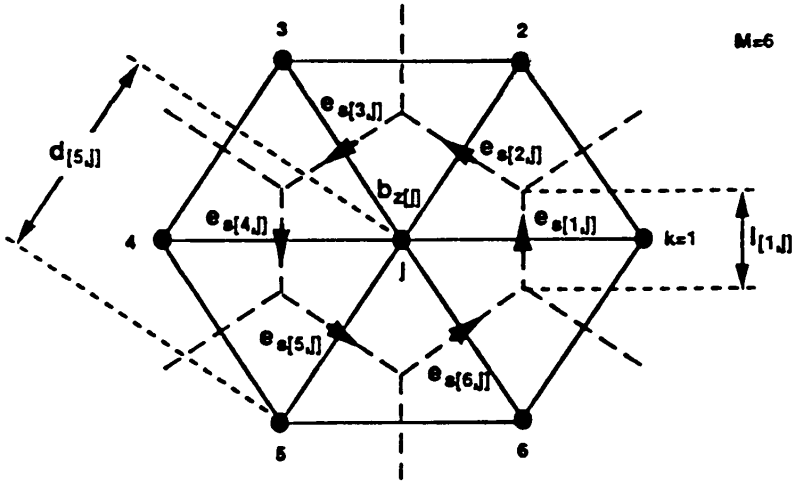

Figure 11.4.5 Field locations in a control region for magnetic field polarization.

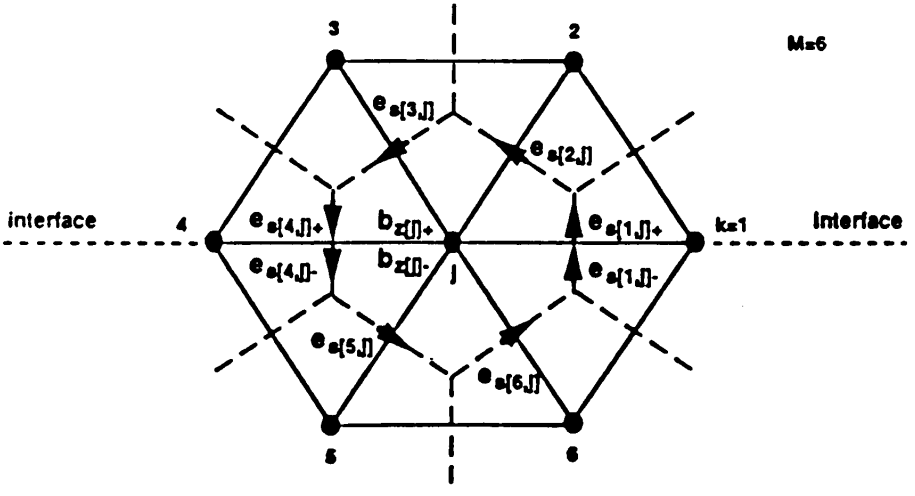

Figure 11.4.6 Field locations on the interface for magnetic field polarization.

Maxwell's equations, written in terms of the normalized variables, for magnetic field polarization are:

$$\nabla_T \times (\hat{n} e_n + \hat{s} e_s) = -\hat{z} \frac{\partial b_z}{\partial \tau} \tag{11.4.30}$$

$$\frac{\partial h_z}{\partial n} = -\frac{\partial d_s}{\partial \tau} \tag{11.4.31}$$

$$\frac{\partial h_z}{\partial s} = \frac{\partial d_n}{\partial \tau} \tag{11.4.32}$$

Applying an area integral and Green's theorem to (11.4.30), e_n and d_n are decoupled from the other field variables and the following equations are obtained:

$$\oint e_s \, dl = -\iint \frac{\partial b_z}{\partial \tau} \, dA \tag{11.4.33}$$

$$\frac{\partial h_z}{\partial n} = -\frac{\partial d_s}{\partial \tau} \tag{11.4.34}$$

Figure 11.4.5 shows the field locations in the control region. $\bar{e}$ and $\bar{d}$ are at the same location, and similarly $\bar{h}$ and $\bar{b}$ are at the same location. Equation (11.4.33) and (11.4.34) are discretized as follows

$$\sum_{k=1}^{M} e_{s[k,j]}^{m-1} \, l_{[k,j]} = \frac{A}{\Delta_\tau} \left(b_{z[j]}^{m-1/2} - b_{z[j]}^{m-3/2} \right) \tag{11.4.35}$$

$$\frac{1}{d_{[k,j]}} \left(h_{z[k]}^{m-1/2} - h_{z[j]}^{m-1/2} \right) = -\frac{1}{\Delta_\tau} \left(d_{s[k,j]}^{m} - d_{s[k,j]}^{m-1} \right) \tag{11.4.36}$$

At the dispersive medium interface, similar to the electric field polarization case, b_z is split into b_{z+} and b_{z-} and e_s is split into e_{s+} and e_{s-}. Figure 11.4.6 shows the field location assignment at the interface. With this field location assignment, the discretization of (11.4.33) and (11.4.34) are

$$\sum_{k=1}^{M} e_{s\pm[k,j]}^{m-1} \, l_{[k,j]\pm} = -\frac{A_+}{\Delta_\tau} \left(b_{z[j]+}^{m-1/2} - b_{z[j]+}^{m-3/2} \right) - \frac{A_-}{\Delta_\tau} \left(b_{z[j]-}^{m-1/2} - b_{z[j]-}^{m-3/2} \right) \tag{11.4.37}$$

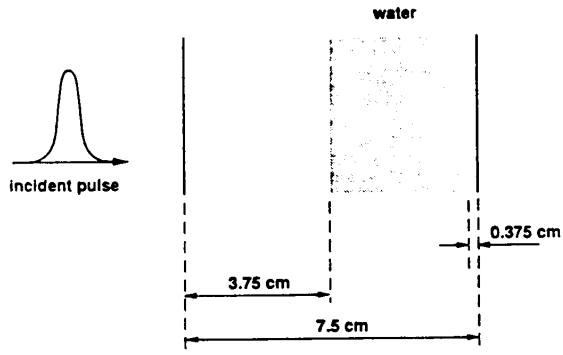

Figure 11.4.7 Geometrical configuration for pulse incident on half space filled with water.

$$\frac{1}{d_{[k,j]}}\left(h_{z[k]}^{m-1/2} - h_{z[j]}^{m-1/2}\right) = -\frac{1}{\Delta_\tau}\left(d_{s[k,j]}^{m} - d_{s[k,j]}^{m-1}\right) \qquad (11.4.38)$$

The two unknowns ($b_{z[j]+}$ and $b_{z[j]-}$) in (11.4.37) are related by the continuity of tangential magnetic field and the materials models on both sides of the interface. The material models on both sides of the interface are also used to calculate e_{s+} and e_{s-}, once d_s is found from (11.4.38).

d. Numerical Results

To illustrate the validity of the FD-TD algorithm for dispersive materials, three numerical examples are considered. In the first and second cases, the configurations are half space filled with dispersive materials and the ratios of the reflected field amplitudes to the incident field amplitudes are calculated. These two cases primarily demonstrate the FD-TD algorithm and the discretization of two models (11.4.14) and (11.4.16). In the third case, the FD-TD algorithm is applied to a 2D electromagnetic scattering problem. The configuration considered in this case is a conducting cylinder coated with a dispersive material. The amplitude of the backscattered fields at a range of frequencies are calculated using the FD-TD technique and compared with those obtained using the eigen function expansion. In this case, the FD-TD algorithm and the triangular grid discretization are employed and tested for their applications to 2D problems.

In the first case, the FD-TD algorithm is applied to the problem of half space filled with water [15]. Figure 11.4.7 shows the configura-

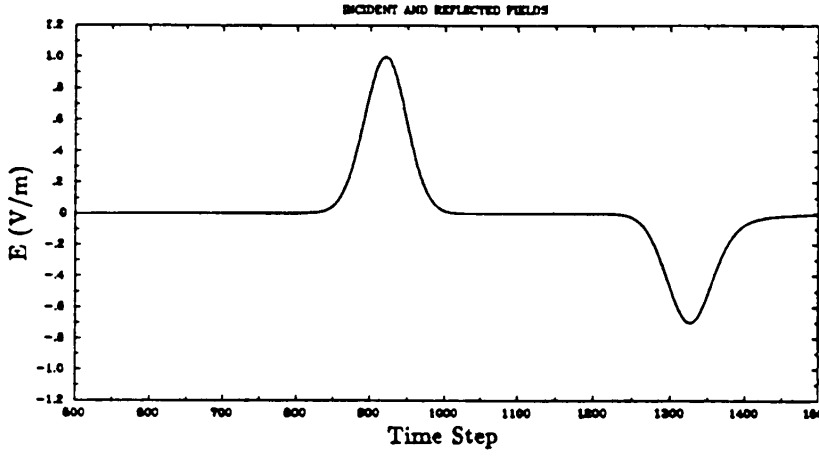

Figure 11.4.8 Incident and reflected electric pulses near air-water interface.

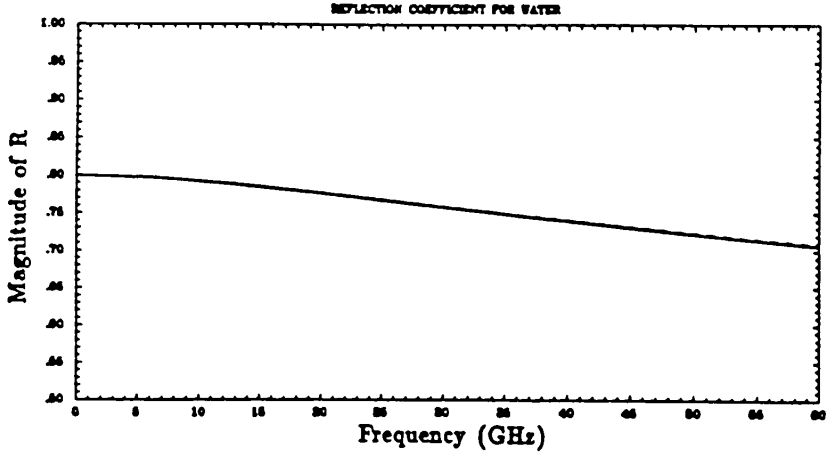

Figure 11.4.9 Reflection coefficient for half space filled with water.

tion for the numerical simulation. The relative permittivity is modeled using the Debye formula (Fig. 11.4.2) with the time domain model of (11.4.16). The incident wave is a Gaussian time pulse centered at DC with a half power bandwidth of 73.4 GHz and an amplitude of 1 V/m. The computational domain is located from the origin to $x = 7.5$ cm and discretized into 1000 divisions. To simulate the half space, a relatively thick medium, from 3.75 cm to 7.125 cm, is chosen so that the transmitted field is significantly attenuated before arriving at the second boundary. The computational domain is truncated by imposing the first order absorbing boundary condition [30,33] at $x = 7.5$ cm. It should be pointed out that the pulse reflected at the artificial boundaries is not only negligible but also separated in time with respect to the reflected pulse at the first boundary. The incident Gaussian time pulse is launched at $x = 0.0$ cm. To eliminate reflection from the source, the first order absorbing boundary condition is imposed after the main portion of the Gaussian time pulse has left the source plane. The normalized time step is chosen to be half the grid size [39]. Figure 11.4.8 shows the incident and reflection pulses at $x = 3$ cm. The incident pulse is centered at about time step of 920 and the reflected pulse is at about 1325 time step. By applying Fourier transforms to the incident and the reflected pulses and taking the ratios for the corresponding frequency components, the reflection coefficient as a function of frequency (from 0 to 60 GHz), is obtained. The results are presented in Fig. 11.4.9 where the solid curve represents the exact solution:

$$R(\omega) = \frac{1 - \sqrt{\epsilon(\omega)\,\mu(\omega)}}{1 + \sqrt{\epsilon(\omega)\,\mu(\omega)}} \tag{11.4.39}$$

The dashed curve shows the calculated reflection coefficients using the FD-TD technique. As seen from Fig. 11.4.9, the calculated result agrees very well with the exact result. This example demonstrates the validity and the accuracy of the FD-TD algorithm, discretization scheme, and the time domain modeling of the Debye's formula.

In the second case, the FD-TD algorithm is applied to the problem of half space filled with relative permeability of 1.0 and relative permittivity given by Fig. 11.4.1. Figure 11.4.11 shows the configuration for the numerical simulation. The time domain model of (11.4.14) is used. The incident wave is a Gaussian pulse centered at 10 GHz with a half power bandwidth of 16.0 GHz and an amplitude of 1 V/m. The computational domain is located from the origin to $x = 15.0$ cm and

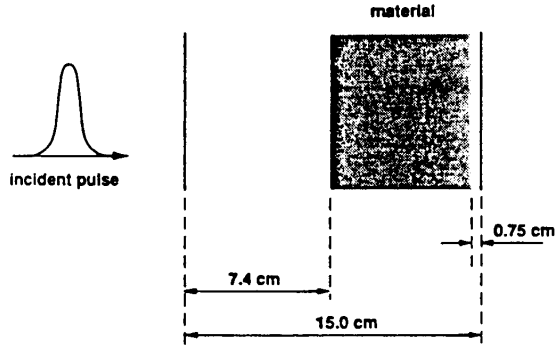

Figure 11.4.10 Geometrical configuration for pulse incident on half space filled with sample dispersive material.

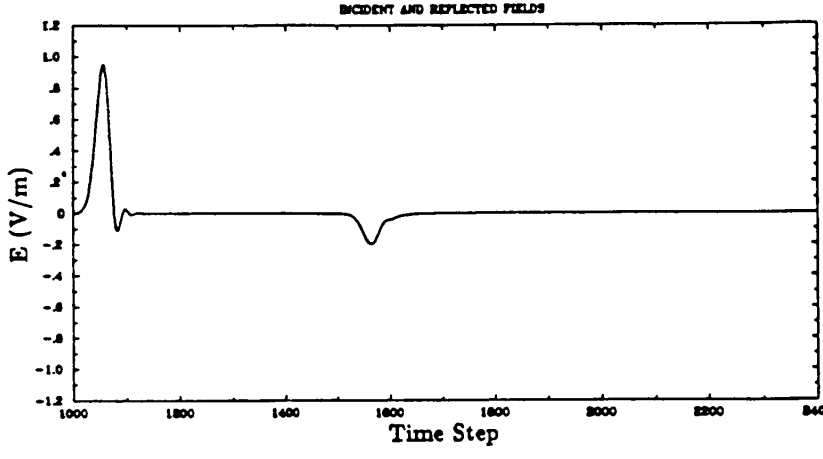

Figure 11.4.11 Incident and reflected electric pulses near air-material interface.

discretized into 1000 divisions. To simulate the half space, a relatively thick medium, from 7.5 cm to 14.25 cm, is chosen so that the transmitted field is significantly attenuated before impinging on the second boundary. The computational domain is truncated by imposing the first order absorbing boundary condition at $x = 15.0$ cm. The inci-

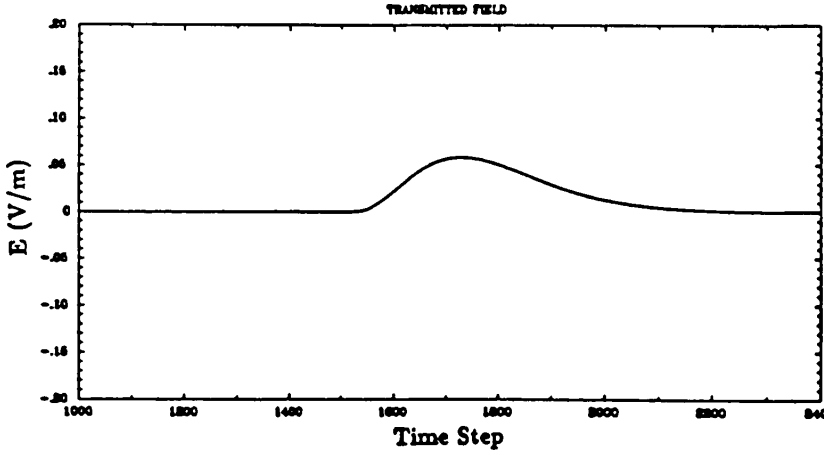

Figure 11.4.12 Transmitted electric pulse near air-material interface.

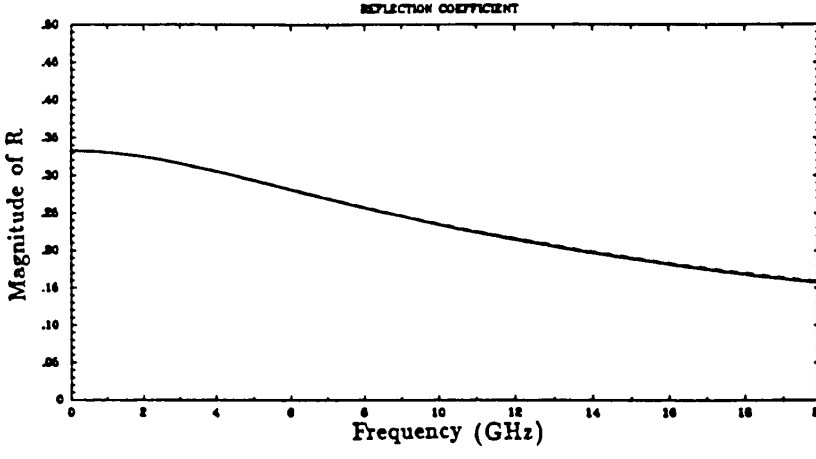

Figure 11.4.13 Reflection coefficient for half space filled with dispersive material.

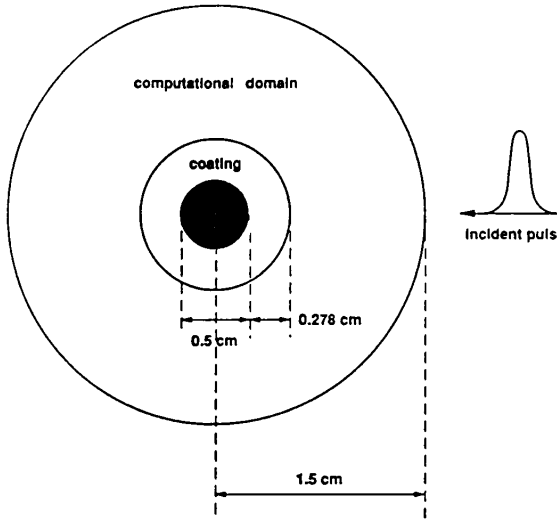

Figure 11.4.14 Geometrical configuration for coated cylinder problem.

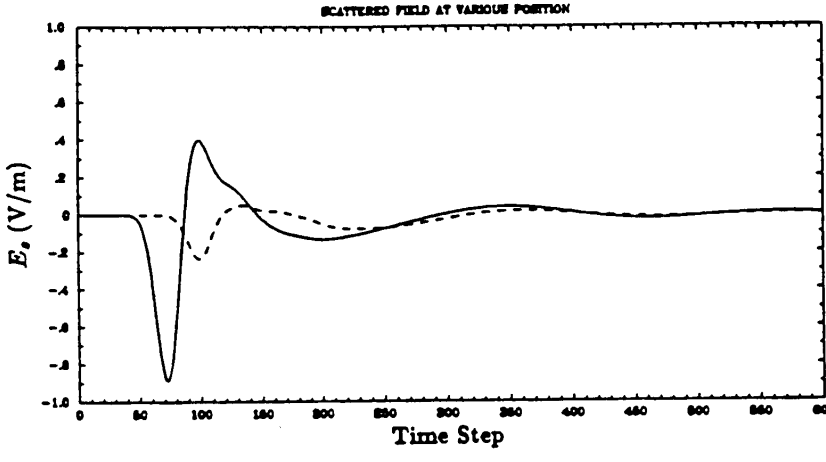

Figure 11.4.15 Electric field amplitudes at r=0.42 cm and r=1.25 cm.

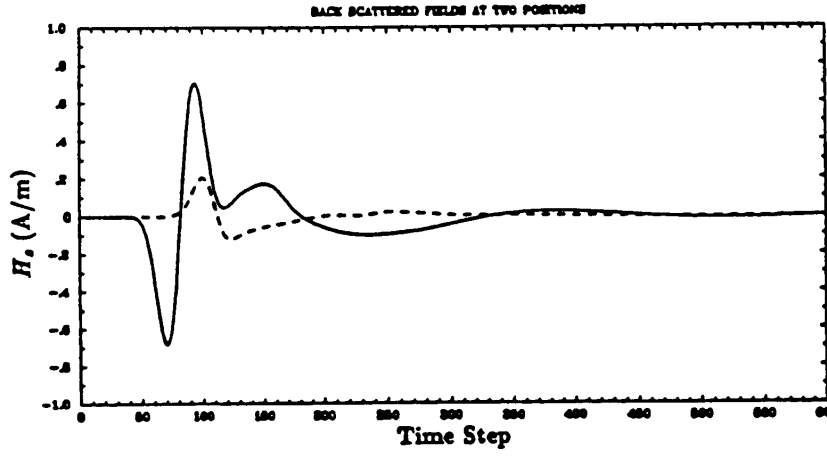

Figure 11.4.16 Magnetic field amplitudes at r=0.42 cm and r=1.25 cm.

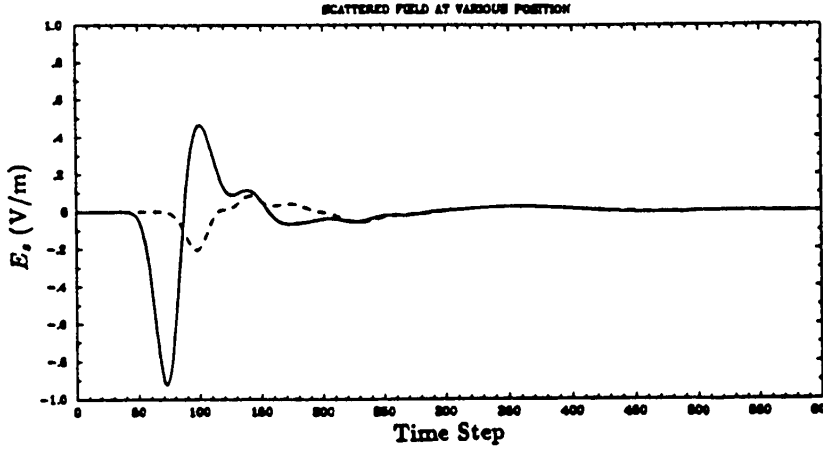

Figure 11.4.17 Electric field amplitudes at r=0.42 cm and r=1.25 cm, (constant magnetic loss).

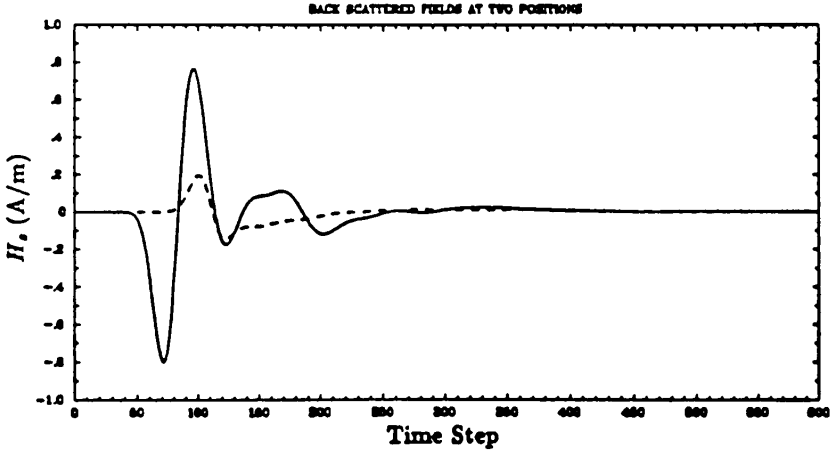

Figure 11.4.18 Magnetic field amplitudes at r=0.42 cm and r=1.25 cm, (constant magnetic loss).

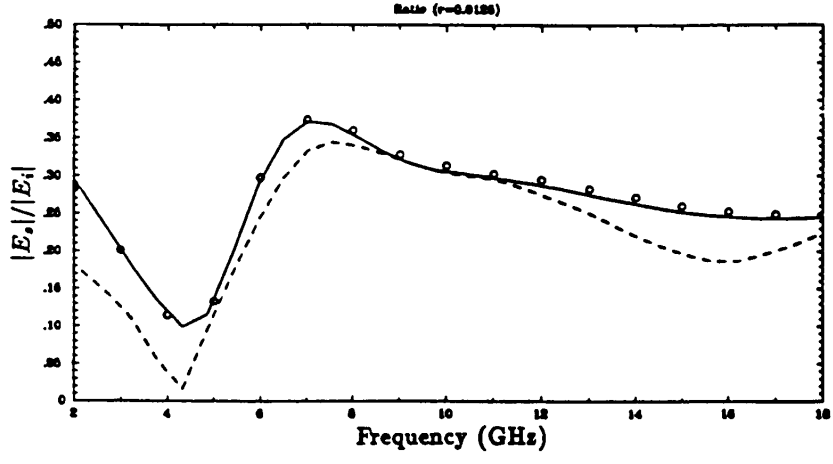

Figure 11.4.19 Ratio of back scattered electric field to incident electric field at r=1.25 cm.

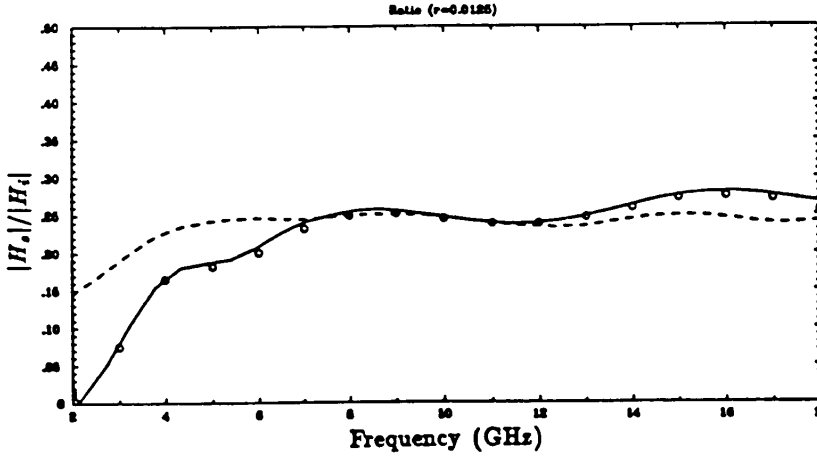

Figure 11.4.20 Ratio of back scattered magnetic field to incident magnetic field at r=1.25 cm.

dent Gaussian time pulse is launched at $x = 0.0$ cm. The normalized time step is chosen to be half the grid size. Figure 11.4.11 shows the incident and reflected pulses at $x = 6.0$ cm. Figure 11.4.12 shows the transmitted pulse at $x = 9.0$ cm. As seen from Fig. 11.4.12, the transmitted pulse is attenuated due to loss and broadened in time due to dispersion. In Figure 11.4.11, the incident pulse is centered at about time step of 1050 and the reflected pulse is at about 1550 time step. By applying Fourier transforms to the incident and the reflected pulses and taking the ratios for the corresponding frequency components, the reflection coefficient as a function of frequency, 2 to 20 GHz, is obtained (Fig. 11.4.13). The solid curve shown in Fig. 11.4.13 represents the exact solution. The dashed curve shows the reflection coefficient calculated using the FD-TD technique. This example again demonstrates the validity and the accuracy of the FD-TD algorithm, discretization scheme, and the time domain modeling (11.4.19) for (11.4.6).

In the last numerical simulation, the 2D dispersive scatterer is considered. Figure 11.4.14 depicts the configuration. The scatterer is a conducting cylinder of 0.5 cm diameter and coated with 0.287 cm thick dispersive material. The coating has constant relative permittivity of

13.2 and relative permeability given by (11.4.7) with parameters given by (11.4.8). The relative permeability of this material as function of frequency is shown in Fig. 11.4.1. The computational domain has radius of 1.5 cm where the time domain Bayliss and Turkel's absorbing boundary condition [39,33] is imposed. The discretization is on triangular grids. A Gaussian pulse with center frequency of 10 GHz and a half power bandwidth of 16 GHz is impinging on the coated cylinder from the positive x axis. The FD-TD algorithm is applied to compute the transient fields in the computational domain. Figures 11.4.15 and 11.4.16 show the backscattered field amplitudes at two locations for the electric and magnetic field polarizations, respectively. The dashed curve corresponds to the field at location inside the coating ($r = 0.42$ cm). The solid curve corresponds to the field at location outside the coating ($r = 1.25$ cm). In order to evaluate the numerical scheme and isolate the effects due to geometry and dispersive material, the FD-TD algorithm with a constant magnetic conductivity of $\sigma_m = 9.475\,\mathrm{k}\Omega/\mathrm{m}$ is also applied. The value of the magnetic conductivity is derived from the imaginary part of the relative permeability at 10 GHz, which is the center frequency in the frequency range of interest. Figures 11.4.17 and 11.4.18 show the corresponding fields at the same two locations for the electric and magnetic field polarizations, respectively. In calculating these results, the dimension of the sides of the triangular cells are approximately 500 microns and the size of the normalized time steps are 222.22 microns. In order to verify the accuracy, Fourier transform is applied to the fields at $r = 1.25$ cm. Figures 11.4.19 and 11.4.20 show the ratio of the magnitudes of the backscattered fields to the incident fields for frequencies ranging from 2 to 18 GHz for the electric and magnetic field polarizations, respectively. The 'o' represents results calculated using eigen function expansion [57]. The solid curves are results calculated using the FD-TD technique in (11.4.11). The dashed curves are obtained using the FD-TD technique with constant magnetic conductivity. As seen from Fig. 11.4.19 and Fig. 11.4.20, the FD-TD technique with proper treatment of dispersion yields much more accurate results than the constant conductivity model, as expected.

11.5 Summary

In this chapter, several implementation-related issues of the FD-TD and FD-FD techniques are discussed. In particular, the absorbing boundary conditions (ABC), FD-TD technique on triangular grids, and application of the FD-TD technique to problems involving frequency dispersive materials are discussed.

The modified pseudo-differential operator technique is discussed and applied to derive the ABC on circular and elliptical boundaries. In the case of the circular boundary, the ABC derived has higher absorbability than the result obtained by Engquist and Majda, and Sommerfeld's radiation boundary condition is naturally contained in the first order term. With a convenient change of variable, the pseudo-differential operator technique is applied to obtain the ABC of the elliptic boundary. The ABC for the elliptical boundary is numerically demonstrated in the frequency domain. It is found that the application of the ABC can potentially offer substantial reduction in computer resource requirements for elongated scatterers.

The finite-difference time-domain technique on triangular grids is developed and verified using various test cases. This technique is the generalization of the control region approximation and the finite difference technique for rectangular grid. The discretization scheme is simple, and reduces to Yee's algorithm when the Dirichlet tessellation becomes rectangular. The discretization is accurate to second order in time and space when the grid is regular. In the case of irregular grid, a first order accurate scheme is obtained. The algorithm can be applied to arbitrary geometries and can handle dielectric/magnetic materials. The algorithm is tested with circular cylinder and strip geometries. The time harmonic results are extracted from the late time responses of sinusoidal excitations and compared with the eigen series solutions for the circular cylinder geometries. For the strip configuration, the computation domains are truncated using either circular or elliptical outer boundaries. Numerical results indicate the highly absorbing nature of corresponding absorbing boundary conditions. For elongated scatterers, the use of the elliptical boundary can reduce the computational domain. Pulse responses are also calculated for the strip configuration to illustrate the time-domain transient analysis.

The FD-TD technique for electromagnetic problems is generalized to handle frequency dispersive materials. Discretization schemes and

effective time domain models are investigated and demonstrated numerically. Numerical results confirm the validity and accuracy of the algorithm. To apply the algorithm, proper frequency domain models for the dispersive materials, such as the Lorentz model and the Debye model, are used. The frequency domain models are then transformed to the time domain model which are in the form of ordinary time differential equations relating $\overline{D}$ to $\overline{E}$ and $\overline{B}$ to $\overline{H}$. To treat the frequency dispersive materials, the conventional FD-TD algorithms for electromagnetic problems are extended. The algorithm is efficient in terms of computation time and memory requirements. Although the algorithm is only demonstrated in 1D and 2D, it can be easily applied to 3D problems.

Acknowledgments

This work was supported by United Technologies Research Center, WaveTracer Contract, Digital Equipment Corporation Contract, NSF Grant 8620029-ECS, and ARO Contract DAAL03-88-J-0057.

References

[1] Yee, K. S., "Numerical solution of initial boundary value problems involving Maxwell's equation in isotropic media," *IEEE, Trans. Ant. Prop.,* **AP-14**, 302–307, May 1966.

[2] Holland, R., and L. Simpson, "Implementation and optimization of the thin-strut formalism in THREDE," *IEEE Trans., Nuclear Sci,* **NS-6**, 1625–1630, 1980.

[3] Holland, R., L. Simpson, and K. S. Kunz, "Finite difference analysis of EMP coupling to lossy dielectric structures," *IEEE Trans. Electromagn. Compat.,* **EMC-22**, 203–209, 1980.

[4] Holland, R., "Finite-difference solution of Maxwell's equations in generalized nonorthogonal coordinates," *IEEE Trans. Nuclear Science,* **NS–30**, 6, 4589–4591, 1983.

[5] Holland, R., "Threds: A finite-difference time-domain EMP code in 3D spherical coordinates," *IEEE Trans. Nuclear Science,* **NS–30**, 6, 4592–4595, 1983.

[6] Ray, S. L., "New general grid finite difference time domain methods for Maxwell's equations in two dimensions," *URSI Radio Science meeting,* Syracuse, New York, 1988

[7] Madsen, N. K., and R. W. Ziolkowski, "Numerical solution of Maxwell's equations in the time domain using irregular nonorthorgonal grids," *Wave Motion,* **10**, 583–596, 1988.

[8] Ziolkowski, R., N. K. Madsen, and R. Carpenter, "Three dimensional computer modeling of electromagnetic fields: global look-back lattice truncation scheme," *J. of Comp. Physics* **50**, 360–408, 1983.

[9] McCartin, B., G. Meltz, R. Mittra, and L. Bahrmasel, "Application of the control region approximation in conjunction with absorbing boundary conditions to the direct solution of electromagnetic scattering problems," *URSI Radio Science meeting,* Syracuse, New York, **14**, 1988.

[10] Meltz, G., B. McCartin, and L. Bahrmasel, "Application of the control region approximation to electromagnetic scattering," *Proc. 1987 URSI Radio Science meeting,* Blacksburg, Virginia, **185**, 1987.

[11] McCartin, B., and J. Dicello, "Three dimensional finite difference frequency domain scattering computation using the control region approximation," *IEEE, Trans. Magnetics,* 1989.

[12] Taflove, A., K. R. Umashankar, and T. G. Jurgens, "Validation of FD-TD modeling of the radar cross section of three-dimensional structures spanning up to nine wavelengths," *IEEE Trans. Ant. Prop.,* **AP-33**, 662–666, June 1985.

[13] Taflove, A., and M. Brodwin, "Numerical solution of steady-state electromagnetic scattering problems using the time dependent Maxwell's equations," *IEEE Trans. Microwave Theory Tech.,* **MTT-23**, 623–630, Aug. 1975.

[14] Taflove, A., and K. R. Umashankar, "The finite-difference time-domain (FD-TD) method for electromagnetic scattering and interaction problems," *J. of Electromagnetic Waves and Applications,*

1, 3, 243–267, 1987.

[15] Luebbers, R. J., F. P. Hunsberger, and K. S. Kunz, "FD-TD formulation for frequency dependent permittivity," *Proc. 1989 URSI Radio Science meeting,* San Jose, California, 50, 1989.

[16] Lee, C. F., R. T. Shin, J. A. Kong, and B. McCartin, "A finite-difference time-domain technique on triangular grid," to be published in *J. of Electromagnetic Waves and Applications.*

[17] Lee, C. F., R. T. Shin, J. A. Kong, and B. McCartin, "A finite difference time domain technique on triangular grids," *PIERS 1989* Boston, MA., July, 1989.

[18] McDonald, B. H., and A. Wexler, "Finite element solution of unbounded field problems," *IEEE Trans, Microwave Theory Tech.,* **MTT-20**, 841–847, 1972.

[19] Morgan, M., and K. K. Mei, "Finite element computation of scattering by inhomogeneous penetrable bodies of revolution," *IEEE Trans. Antennas Propagat.,* **AP-27**, 1979.

[20] Kashiwa, T., N. Yoshida, and I. Fukai, "Transient analysis of a magnetized plasma in three dimensional space," *IEEE Trans. Ant. Prop.,* **AP-36**, 1096–1105, August 1988.

[21] Kunz, K. S., and K. Lee, "A three dimensional finite-difference solution of the external response of an aircraft to a complex transient EM environment: Part I – The method and its implementation," *IEEE Trans. Electromagn. Compat.,* **EMC-20**, 328–333, 1978.

[22] Taflove, A., and M. Brodwin, "Computation of the electromagnetic fields and induced temperatures within a model of the microwave-irradiated human eye," *IEEE Trans. Microwave Theory Tech.,* **MTT-23**, 888–896, Nov. 1975.

[23] Gandhi, O. P., "Numerical method for design of electromagnetic hyperthermia," *PIERS 1989* Boston, MA., July, 1989.

[24] Gwarek, W. K., "Analysis of arbitrarily shaped two-dimensional microwave circuits by finite-difference time-domain method," *IEEE Trans.,* **MTT-36**, 738–744, 1988.

[25] Olivier, J. C., and D. A. McNamara, "Finite-difference time-do -main (FD-TD) analysis of discontinuities in homogeneous, dispersive waveguides," *Electronic Letter,* **25**, 15, 1006–1007, 1989.

[26] Reineix, A., and B. Jecko, "Analysis of microstrip patch antennas using finite-difference time-domain method," *IEEE. Trans. Ant. Prop.,* **AP-37**, 11, 1361–1369, 1989.

[27] Fusco, M., "FD-TD algorithm in curvilinear coordinates," *IEEE. Trans. Ant. Prop.,* **AP-38**, 1, 76–89, 1990.

[28] Mei, K. K., "Unimoment method of solving antenna and scattering problems," *IEEE. Trans. Ant. Prop.,* **AP-22**, 6, 760–766, 1974.

[29] Ting, L., and M. Miksis, "Exact boundary conditions for scattering problems," *J. Acoust. Soc. Am.,* **80(6)**, 1986.

[30] Engquist, B., and A. Majda, "Radiation boundary conditions for the numerical simulation of waves," *Math. Comp.,* **31**, 629–651, 1977.

[31] Majda, A., and S. Osher, "Reflection of singularities at the boundary," *Comm. on Pure and Applied Math.,* **28**, 479–499, 1975

[32] Mur, G., "Absorbing boundary conditions for the finite difference approximation of the time domain electromagnetic field equations," *IEEE Trans. Elec. Comp.,* **EMC-23**, 4 Nov. 1981.

[33] Bayliss, A. and E. Turkel, "Radiation boundary conditions for wave-like equations," *Comm. Pure Appl. Math.,* **33**, 707–725, 1980.

[34] Bayliss, A., C. Goldstein, and E. Turkel, "On accuracy conditions for the numerical computation of waves," *J. Comp. Phys.,* **59**, 396–404, 1985.

[35] Bayliss, A., M. Gunzburger, and E. Turkel, "Boundary condition for the numerical solution of elliptic equations in exterior regions," *SIAM J. Applied Math.,* **12**, 430–451, 1982.

[36] Blaschak, J. G., and G. A. Kriegsmann, " A comparative study of absorbing boundary conditions," *J. Comput. Phys.,* **77**, 109–139, 1988.

[37] Moore, T. G., J. G. Blaschak, and G. A. Kriegsmann, "Theory and application of radiation boundary operators," *IEEE Trans. Ant. Prop.,* **Vol AP-36**, 12, 1988.

[38] Lee, C. F., R. T. Shin, J. A. Kong, and B. McCartin, "Absorbing boundary conditions on circular and elliptical boundaries," *PIERS 1989* Boston, MA., July, 1989.

[39] Lee, C. F., R. T. Shin, J. A. Kong, and B. McCartin, "Absorb-

ing boundary conditions on circular and elliptic boundaries," *J. Electromagn. Wave and Appl.*, accepted for publication, 1989.

[40] Halpern, L., and L. Trefethen, "Wide angle one way wave equations," *J. Acoust. Soc. Am.*, 1397–1404, 1986.

[41] Trefethen, L. N., and L. Halpern, " Well-posedness of one-way wave equations and absorbing boundary conditions," *Math. Comput.*, **47**, 176, 421–435, 1986.

[42] Ramahi, O., and R. Mittra, "A systematic approach to improving the solution based on the absorbing boundary condition," *Proc. 1988 URSI Radio Science Meeting,* Syracuse, New York, 1988.

[43] Higdon, R., "Absorbing boundary conditions for difference approximations to the multi-dimensional wave equation," *Math. Comp.*, **47**, 437–459, 1986.

[44] Wagatha, L., "Approximation of pseudo-differential operators in absorbing boundary conditions for hyperbolic equations," *Numerical Math.*, **42**, 51–64, 1983.

[45] Lindman, E., "Free space boundary conditions for the time dependent wave equation," *J. Comp. Physics* **18**, 66–78, 1975.

[46] Bevensee, R. M., "Time domain radiation boundary conditions obtained from 'backward' solutions of the space time wave equation," Lawrence Livermore National Laboratory Report, 1988.

[47] Kriegsmann, G. A., and C. Morawetz, "Solving the Helmholtz equation for exterior problems with variable index of reflection: I," *SIAM J. Sci. Stat. Comput.*, 3, 371–375, 1980.

[48] Merewether, D., R. Fisher, and F. Smith, "On implementing a numeric Huygens' source scheme in a finite difference program to illuminate scattering bodies," *IEEE Trans. Nuclear Sci.*,**NS–27**, 1829–1833, 1980.

[49] Roy, J. E., H. Dennis, and H. Choi, "A simple absorbing boundary algorithm for the FD-TD method with arbitrary incident angle," *Proc. 1987 URSI Radio Science meeting,* San Jose, California, **54**, 1989.

[50] Kriegsmann, G., A. Taflove, and K. R. Umashankar, "A new formulation of electromagnetic wave scattering using an on-surface radiation boundary condition approach," *IEEE Trans. Ant. Prop.*,

AP-35, 2, 153–161, 1987.

[51] Wilcox, C., "An expansion theorem for electromagnetic fields," *Comm. on Pure and Applied Math.,* **9**, 115–134, 1956

[52] Friedrichs, K. O., Pseudo-Differential Operators: An Introduction, Courant Institute of Mathematical Sciences, New York University.

[53] Nirenberg, L., Lectures on Linear Partial Differential Equations, **17**, Regional Conference Series in Mathematics.

[54] Kumano-go, Hitoshi, "Pseudo-differential operators," The M.I.T. press, Cambridge, Massachusetts, and London, England, 1974.

[55] Morawetz, C., and G. Kriegsmann, "The calculations of an inverse potential problem," *SIAM J. Applied Math.,* **43**, 844–854, 1983.

[56] Morawetz, S., and G. A. Kriegsmann, "The calculations of an inverse potential problem," *SIAM J. Applied Math.,* **43**, 844–854, 1983.

[57] Chang, I., "Plane electromagnetic wave scattering from coated cylinders," M.S. Thesis, MIT, 1989.

[58] Rao, S. M., D. R. Wilton, and A. W. Glisson, "Electromagnetic scattering by surfaces of arbitrary shape," *IEEE Trans. Antennas Propagat.,* **AP-30**, 409–418, 1982.

[59] Lee, C. F., R. T. Shin, J. A. Kong, and E. B. Smith, "Application of FD-TD technique to frequency dispersive materials," to be published in *J. of Electromagnetic Waves and Applications.*

[60] Kong, J. A., *Electromagnetic Wave Theory,* Wiley-Interscience, New York, 1986.

[61] Chu, S., and S. Wong, "Linear pulse propagation in an absorbing medium," *Physical Reveiw Letters,* **48**, 11, 738–1293, 1982.

[62] Boll, R., *Soft magnetic materials for telecommunication,* Heyden, London, 1979.

[63] Smit, J., *Magnetic properties of material,* McGraw Hill, New York, 1971.